Extensive air showers and the LPM effect

1. Introduction

Cosmic rays are ionized nuclei that have been accelerated in space up to high energies and reach the Earth. When entering the atmosphere they interact with it and produce cascades of new particles called extensive air showers. Cosmic rays may reach up to 10^{20} eV, an energy above which they interact with the cold (2.7 K) photons of the cosmic microwave background (CMB) to produce pions, thereby loosing energy in the process. This induces an effective cutoff in the energy spectrum of cosmic rays called the GZK cutoff [1] from the name of the physicists who predicted its existence. The flux of cosmic rays that reach the Earth decreases with energy as a power law of index 2.7. At the highest energies, it reaches the very low value of 1/km^2/century, requiring for its detection very large detector coverage. The Pierre Auger Observatory (PAO), with which VATLY – the laboratory where the present work has been done – is associated [2], extends over 3000 km^2 in the Argentinean pampas and is dedicated to the detection and study of the highest energy, so-called ultra-high energy, cosmic rays (UHECR).

UHECR showers cover a few square kilometers when reaching the Earth and include several billions particles, mostly electrons, photons and, to a lesser extent, muons. This coverage and the number of such particles provide a measure of the energy of the shower. Another measure is obtained from the total amount of fluorescence light (near UV) produced by the shower particles in the atmosphere. The relation between these quantities and the cosmic ray energy is obtained from extensive simulations of the shower development process.

At the highest energies a quantum effect, referred to as the Landau-Pomeranchuk-Migdal (LPM) [3] effect from the name of the physicists who predicted it, causes a suppression of some of the cross-sections associated with the shower development, essentially bremsstrahlung and pair creation. As a result, the shower develops over a longer distance than would be predicted by a simulation ignoring the LPM effect. This is of particular importance when aiming at a precise identification of the nature of the primary cosmic rays, precisely at a measurement of their average atomic mass (somewhere between proton and iron). Indeed the main difference between showers induced by a proton and by an iron nucleus of the same energy is that, on average, the latter starts developing at higher altitudes than the former.

The aim of the present work is to evaluate the effect of the LPM suppression on the development of extensive air showers. It makes use of an existing simulation code [4] of the development of electromagnetic showers, i.e. showers induced by an electron or a photon. UHECR showers produce a large quantity of mesons, of which ~ 1/3 are neutral pions which decay promptly into a

photon pair and generate electro-magnetic sub-showers which carry a large fraction of the primary energy. Including the LPM suppression in the expressions of the bremsstrahlung and pair creation cross-sections allows for an evaluation of its effect on the shower development, the results of which are presented here.

The dissertation is organized as follows: Section 2 is a brief presentation [5] of the physics of UHECR, the mechanism of acceleration and their detection in the PAO. Section 3 describes the development of electromagnetic showers and the code used for its simulation. Section 4 reviews the physics of the LPM effect and the evidence for it. Finally, Section 5 presents the results of the inclusion of LPM suppression in the shower development code. A brief conclusion summarizes the main results.

2. UHECR: acceleration and detection

A BRIEF HISTORY

At the end of the XIXth century, scientists were puzzled by the spontaneous discharge of their electroscopes which suggested the presence of an ionizing radiation. In 1909, Wulf, on the Eiffel tower, noted that the discharge rate was decreasing with altitude. Between 1911 and 1913 the Austrian physicist Viktor Hess (Figure 1) performed balloon measurements reaching up to five kilometres in altitude and established the existence of an "unknown penetrating radiation coming from above and most probably of extraterrestrial origin". He shared the 1936 Nobel Prize with Carl Anderson. In the following years cosmic rays became the subject of intense research, in particular with Millikan (who coined the name in 1925) and Anderson at Pikes peak. In 1927 the dependence on latitude and east-west asymmetry established unambiguously that cosmic rays were charged particles, not photons. In 1938, Pierre Auger, using counters in coincidence, discovered extensive air showers and understood that they were produced by very high energy (up to 10^{15}eV) primaries interacting with the Earth atmosphere.

Figure 1: The pioneers (from left to right): Viktor Hess and his balloon, Pierre Auger at the Jungfraujoch, and Anderson with his cloud chamber.

In the thirties and forties, when accelerators were not yet dominating the scene, cosmic rays became the laboratory for the study of particle physics. Anderson discovered the positron in 1932 and the muon in 1938. Powell and Occhialini discovered the pion in 1947. Then came strange particles: kaons, hyperons and many others. In the fifties, accelerators took over and cosmic rays got studied for their own sake.

For many years following, major effort was devoted to the study of cosmic rays, trying to understand their origin. Ground detectors, large arrays and fluorescence telescopes, reached very high energies (John Linsley at Volcano Ranch saw the first 10^{20} eV shower in 1962). Space astronomy has been a break through for the study of low energy cosmic rays, in particular solar energetic particles (SEP).

In the past 20 years, spectacular progress in astrophysics and long time scales implied in the construction of very high energy accelerators have caused a renaissance of interest in cosmic ray physics under the name of astroparticle physics. In particular, TeV gamma ray detectors have been constructed and operated. Their main asset is that they can point to the sources without suffering deflections from magnetic fields. To study cosmic rays, a new generation of ground detectors was born.

In particular, the Pierre Auger Observatory (Figure 2) is a huge and hybrid detector covering 3000 km^2 where showers are detected from the fluorescence they produce in atmosphere and by their impact on a ground detector array. Data are transferred by radio to an acquisition centre which filters them and sends them to the laboratories associated with this research. The Observatory already reported two important results: it has given evidence for the interaction of ultra high energy cosmic rays (UHECR) with the cosmic microwave background (CMB) and it has shown that at least part, if not all, UHECRs originate from AGN rich regions.

Plans to use the whole Earth atmosphere as a radiator observed from space are being implemented and neutrino astronomy is currently being pioneered.

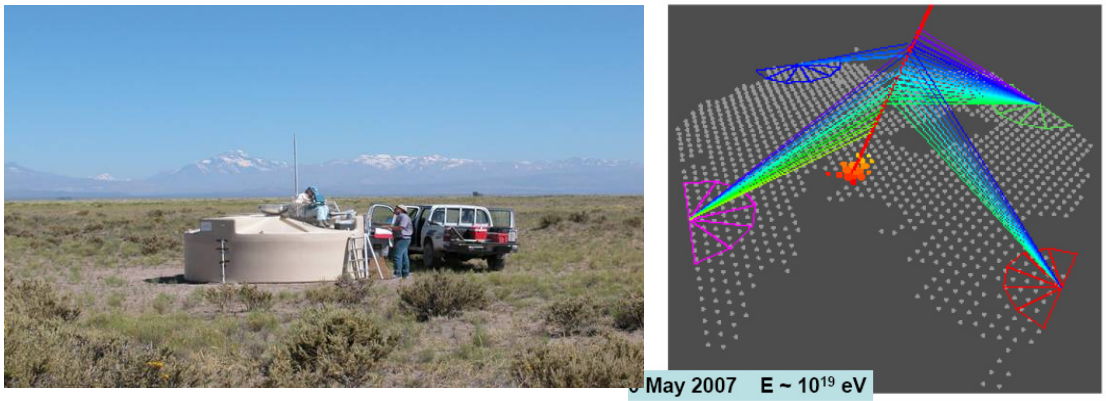

Figure 2: Left: a ground detector of the PAO array; right: a UHECR detected by the PAO ground array and by its four fluorescence eyes.

ENERGY SPECTRUM

Cosmic rays are ionized nuclei that travel in space up to extremely high energies of the order of 10^{20}eV=16 Joules (Figure 3)! There are very few of them but they carry as much energy as the CMB or the visible light or the magnetic fields, namely ~1eV/cm^3. They have a power law energy spectrum spanning 32 decades (12 decades in energy), of the approximate form $E^{-2.7}$.

Whenever they have been measured, cosmic ray abundances are similar to elemental abundances observed in their environment (Figure 4), suggesting that they have been accelerated from interstellar matter. As in any galactic environment, hydrogen and helium dominate, even-even nuclei are naturally favoured and the iron region which corresponds to the strongest nuclear binding is enhanced. The main difference is that the valleys are now filled by spallation reactions on the matter encountered by the cosmic ray during its journey in the interstellar medium, typically ~7 g.cm^{-2}.

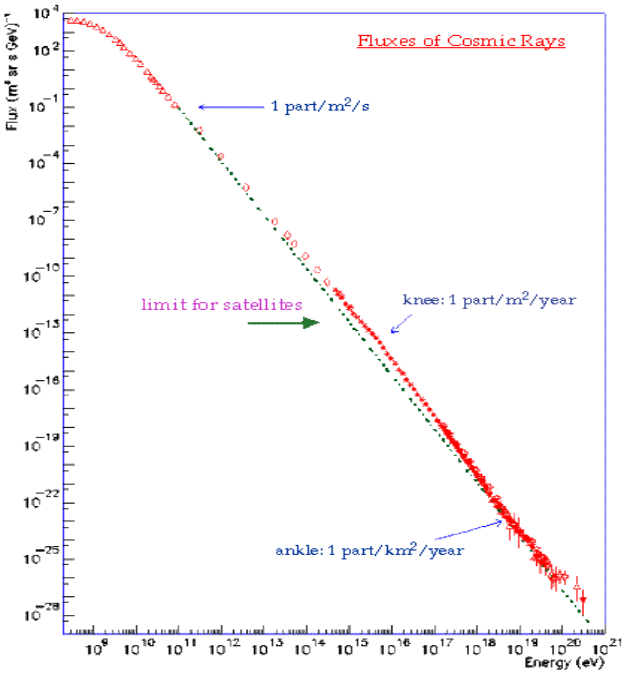

Figure 3: Cosmic ray energy spectrum;

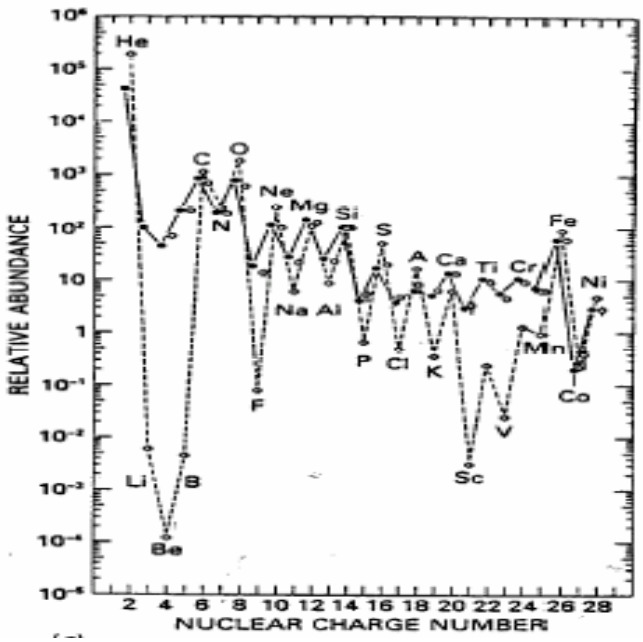

Figure 4: Nuclear abundances

The very low energy part of the cosmic ray spectrum is of solar origin, but most of it does not reach us because of the Earth magnetic shield. From that part of the cosmic ray spectrum which reaches the Earth, one evaluates an energy density ~10^{-12} erg/cm^3. Most of it must have a galactic origin because of the magnetic trapping in the Milky Way disk, corresponding to a galactic escape time of ~3 10^6 y. The cosmic ray power amounts therefore to some ~10^{-26} erg/cm^{3}s which can be compared with the power delivered by supernova explosions, ~10^{51}erg/SN giving, for three SN explosions per century in the disk, ~10^{-25}

erg/cm^{3}s. Namely, galactic cosmic rays carry some ~10% of the power delivered by SN explosions and are indeed found to originate from Super Nova Remnants (SNR, see below).

It is only in the higher energy part (UHECR) of the spectrum that an extra galactic component can be found. Estimating its energy content requires a low energy extrapolation giving an energy density $\rho_{CR} > 2\ 10^{-19} erg/cm^3$. One gets from it an estimate of the power needed: $\rho_{CR}/10^{10}\ y \sim 1.3\ 10^{37}\ erg/Mpc^3/s$. In comparison with Active Galactic Nuclei (AGN) and Gamma Ray Bursts (GRB) energies, a density of $10^{-7}\ AGN/Mpc^3$ implies $>10^{44}\ erg/s/AGN$ in order to reach the same energy density, while for *1000 GRB/y* one needs $>3\ 10^{52} erg/GRB$. Both active galactic nuclei and gamma ray bursts stand, from the point of view of energy, as possible sources of the cosmic ray extra galactic component.

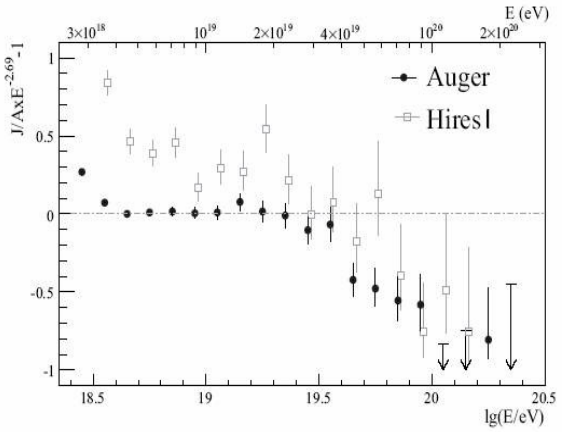

Figure 5: Evidence for the GZK cut-off.

The differential spectral index of the energy spectrum changes at ~ 3 10^{15} eV from 2.7 to 3.0; this is referred to as the knee. It changes again back to 3 at the upper end of the spectrum; this is referred to as the ankle. These deviations from a pure power spectrum are related with the origin of the cosmic rays in the energy intervals of relevance (galactic or extra-galactic) and are not understood in detail; yet, sensible scenarios can be produced which reproduce well the data. Of relevance are the interactions of cosmic rays with the CMB, producing either electron-positron pairs or new mesons. Of these, the pion photoproduction threshold is of particular importance and causes the so-called Greisen-Zatsepin-Kuzmin (GZK) cut-off at the end of the spectrum. Until recently the existence of this cut-off was controversial but the PAO has settled the issue (Figure 5) and given clear evidence for it. With a typical interaction length in the few 10 Mpc scale, cosmic rays coming from larger distances cannot make it to the Earth without interacting, and therefore loose energy: their flux is significantly damped and only nearby (<100 Mpc) sources can contribute to the UHECR spectrum.

GALACTIC SOURCES

Recent progress in gamma ray astronomy has shed much light on the mechanism of acceleration of galactic cosmic rays. Contrary to cosmic rays, gamma rays travel straight in the universe and point back to their sources. They are good at detecting the high energy decay photons coming from neutral pions produced in the interaction of very high energy cosmic rays with interstellar matter.

Figure 6: The High Energy Stereoscopic System (HESS, Namibia) includes four telescopes at the corners of a 120×120 m^2 square, operating above 100 GeV. Its field of view is 5^o and its resolution a few arc minutes. To take a picture of the Crab takes only 30 seconds.

Gamma ray astronomy has shown that many sources have an *X* ray counterpart identified as a Supernova remnant (SNR) and has established that most galactic cosmic rays originate from SNRs. Main sources of high energy photons are bremsstrahlung (synchrotron radiation) at low energies and π^0 decays (hadrons) or inverse Compton on CMB (electrons) at high energies. HESS TeV observations (Figure 6) have revealed numerous shell-type SNRs and established that the shell is the source of the gamma ray signal (Figures 7 and 8).

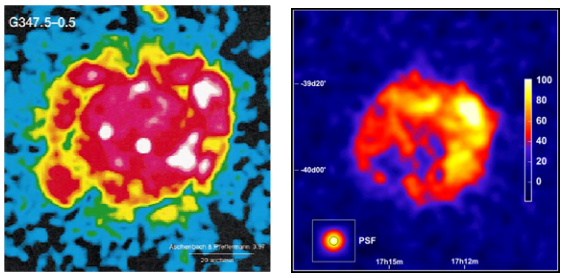

Figure 7: SNR RX J1713 was seen in *X* ray in 1996 by ROSAT (left). The *X* ray spectrum revealed mostly non-thermal *X*-rays and the diameter was measured ~1 kpc. The HESS picture (right) was taken in 2004 and took 33 h live time with all four telescopes. The SNR shell was resolved.

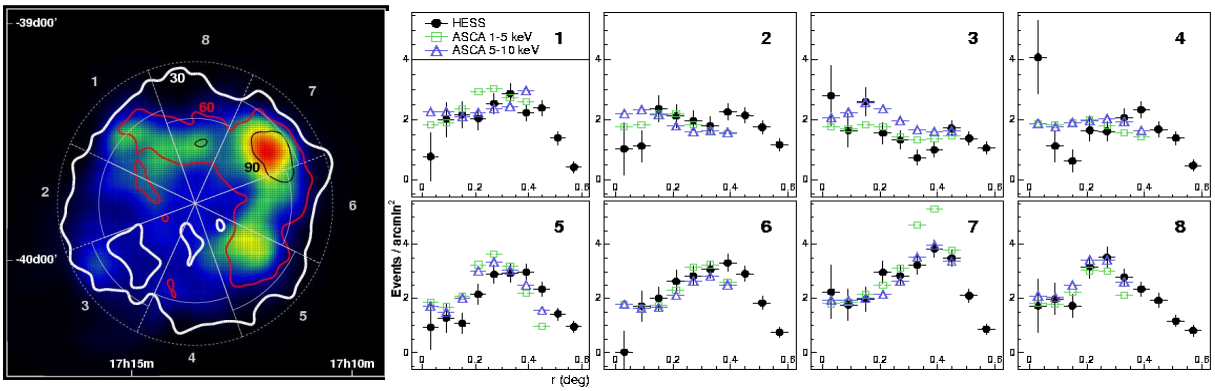

Figure 8: Comparison of radial intensity profiles measured in *X* and γ rays in separate octants of SNR RX J1713. The overall correlation coefficient between the two radial distributions is 80%.

There exist two main types of Supernovae (Figure 9): Ia and II.

Type Ia: a white dwarf, member of a binary, accreting from its companion until reaching Chandrasekhar mass of 1.4 solar masses. The core is fully burned, the SNR shell is empty.

Type II: a massive star collapsing into a neutron star that remains in the centre, possibly detected as a pulsar (Crab) the wind of which gives energy to the remnant (one speaks of a plerion).

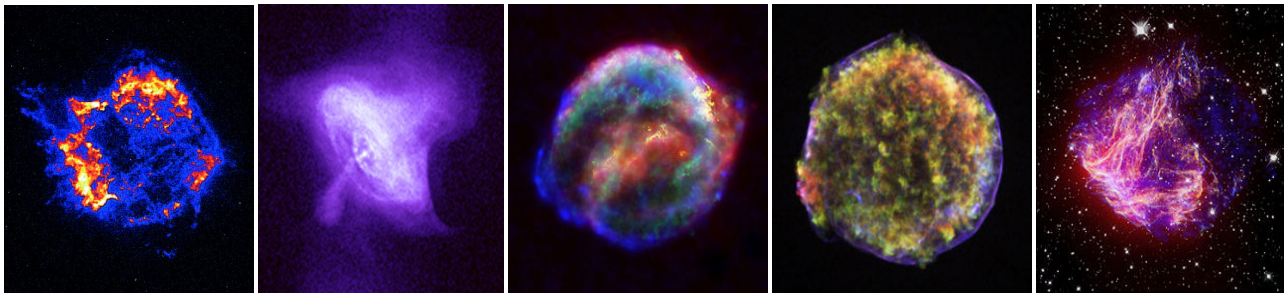

Figure 9: Very high resolution *X* ray images can presently be obtained of SNRs. From left to right: Cassopieia A, the Crab, Kepler (SN 1604), Tycho (SN 1572) and N49.

One understands the details of SNR shell structures as follows (Figure 10):
The explosion blast wave sweeps up the ISM in the forward shock. As mass is swept up, the forward shock decelerates and ejecta (having abundances as in the progenitor) catch up. Then, the reverse shock heats the ejecta and nuclear reactions produce new heavy elements. Once enough mass has been swept up (> 1-5 M_{ej}) the SNR enters the so called Sedov phase and slowly dilutes in the ISM.

While thermal particles and magnetic field are concentrated in the shell, relativistic particles extend to much larger distances and synchrotron emission is confined to magnetic field regions. The shock structure depends on the SNR age: one must distinguish between young and old SNRs. In the case of a plerion, the presence of a pulsar in the centre complicates the situation but the general picture remains unchanged.

The detailed study of the shock region using *X* rays has given evidence for the presence of strong turbulences and an important amplification of the ambient magnetic field (Figure 11). It reaches two orders of magnitude instead of one expected from the hydrodynamic compression.

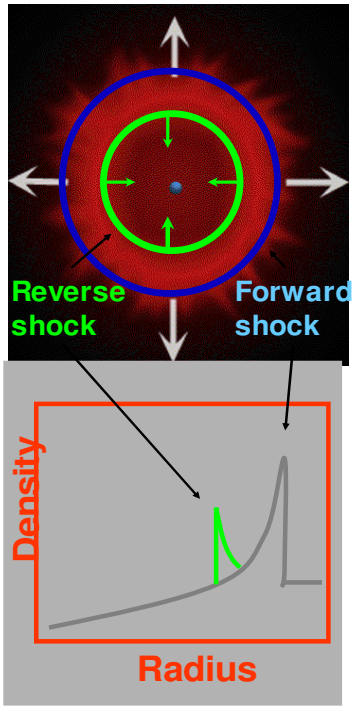

Figure 10: SNR shell structure

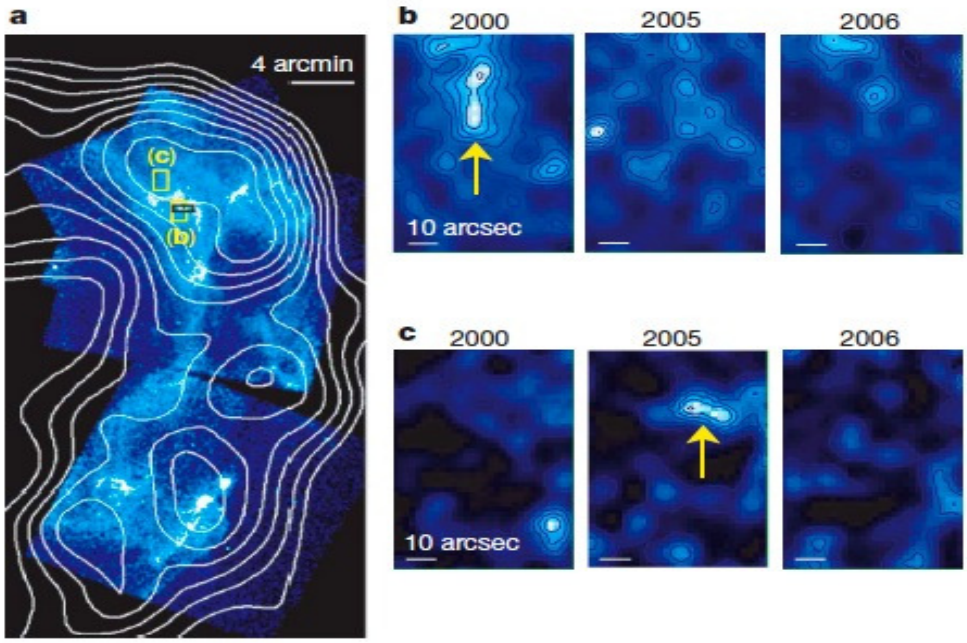

Figure 11: Evidence for time varying turbulences in the shell of RX J1713.

Evidence for magnetic field amplification is obtained from the ratio of radio to TeV emission as a same distribution of electrons produces synchrotron (radio, X-ray) and TeV (Inverse Compton) but synchrotron depends directly on field while IC and pion decays do not. The sharp outer X-ray edges seen in several young SNRs provide additional evidence as shock front compression is a revelator of field amplification.

Cosmic rays and the magnetized plasma carry similar energy densities: they do interact on each other. Accelerated particles tend to stream ahead upstream, which causes the generation of streaming instabilities and makes the evolution non linear, resulting in a strong amplification of the mean field: the structure of the shock is modified by cosmic ray retroaction. The higher field, in turn, depresses Inverse Compton with respect to synchrotron emission, implying faster scattering and increased maximum momentum.

DIFFUSIVE SHOCK ACCELERATION

The above observations make it possible to explain the acceleration of cosmic rays on either side of the shock by a mechanism called diffusive shock acceleration. It is reminiscent of what happens in a cyclotron (Figure 12): the particle is accelerated locally on crossing the shock (equivalent of the gap between the dees) and is guided by magnetic fields on either side in such a way as to come back to the shock (equivalent of the dipole guide field). However both the acceleration and guiding processes are very different from the cyclotron case. Guiding is provided by stochastic collisionless scattering on magnetic turbulences.

Acceleration is best described in the shock frame where both upstream and downstream media move toward each other with large relative velocity β. Hence the energy $E+\Delta E$ of the cosmic ray (mass M) after having crossed the shock is given as a function of its energy E before having crossed the shock as $E+\Delta E = \gamma\beta E+\gamma p$ with $\gamma^2 = \gamma^2\beta^2+1$ and $E^2=p^2+M^2$. As for $\beta<<1$ $\gamma\sim1$ $p=E$ and we get for relativistic cosmic rays: $\Delta E = \beta E+O(\beta^2)$. One speaks of first order Fermi acceleration. $\Delta E/E=\beta$ implies $E_n= E_0(1+\beta)^n$ after n shock traversals. Indeed, when the particle comes back to the shock front, its momentum has changed direction but its energy is still the same because there has been no collision with the ISM which is of such a low density.

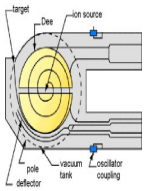

Figure 12: Principle diagram of a cyclotron.

Not static, but continuously recycled through star collapses, the ISM is made of three basic constituents: matter, magnetic fields and cosmic rays. In the Milky Way, it amounts to 10-15% of the disk mass. OB associations and SNs affect the ISM through winds, radiation, heating, ionization and explosions. In practice actual collisions between cosmic rays and ISM can be ignored.

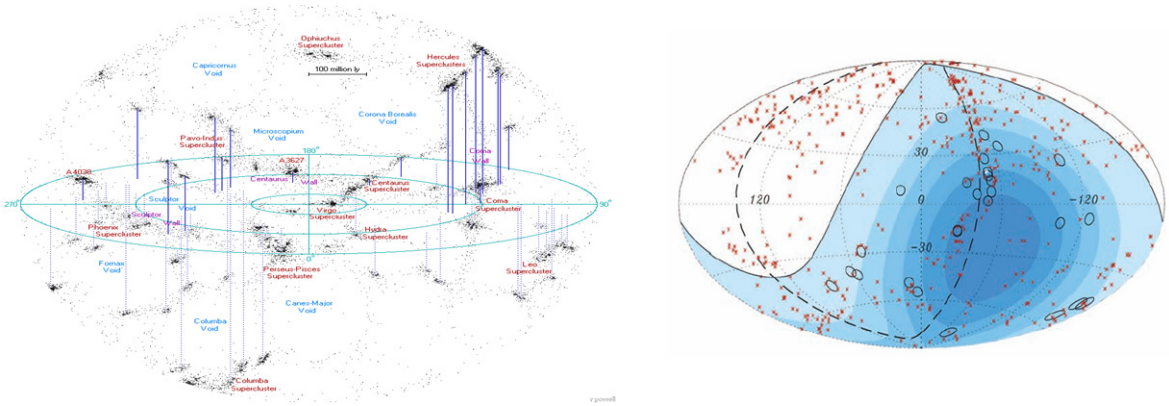

Figure 13: Left: the nearby Universe ; right: Circles of 3.1^o are drawn around 27 UHECR detected by Auger; red crosses are 472 AGN (318 in field of view) having z<0.018 (D<75Mpc). The solid line shows the field of view (zenith angle < 60^o) and the colour tells the exposure. The dashed line is the super galactic plane.

UHECRs

Until recently, it had not been possible to do cosmic ray astronomy because of the images of the sources were blurred by magnetic fields. The large UHECR statistics accessible to the PAO is now making it possible and reveals a clear

correlation with galactic counterparts. Of relevance to this study is the fact that the nearby universe (100 Mpc radius), in which detected UHECRs are confined by the GZK cut-off, is highly inhomogeneous (Figure 13 left).

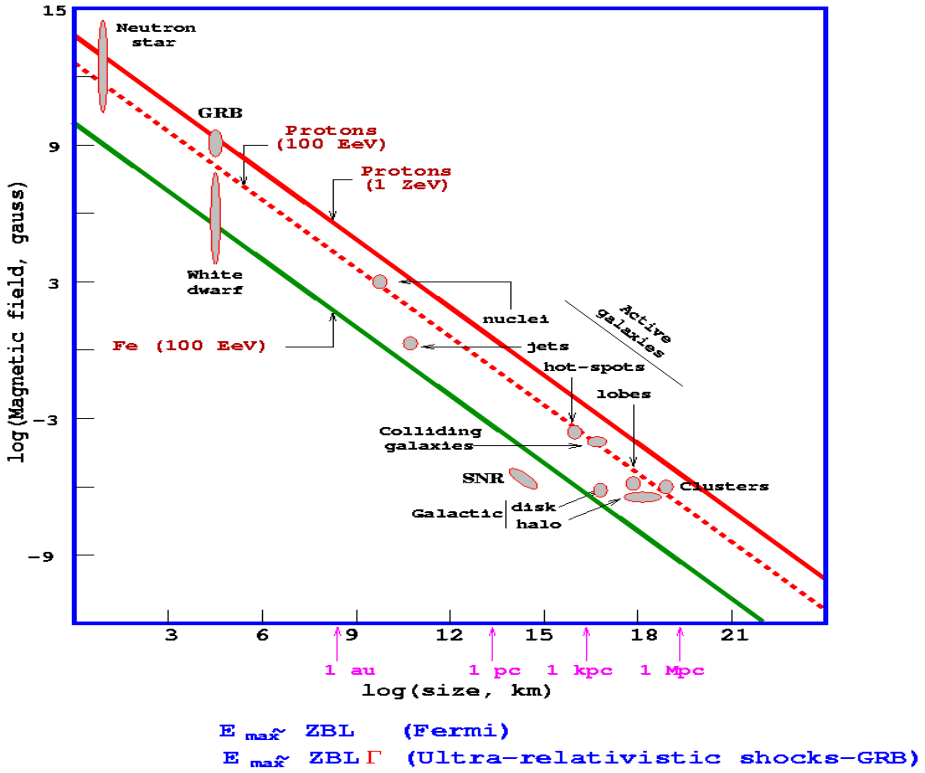

Figure 14: Hillas plot; the upper lines are for protons of 100 and 1000 EeV.

Selecting UHECR observed at the PAO [6] with energy in excess of 6 10^{19} eV (to prevent significant magnetic bending) and comparing the direction in the sky where they come from with a catalogue of nearby (<75 Mpc) galaxies, reveals a strong correlation (Figure 13, right). There is an even better correlation with nearby AGNs (of which, however, we do not have complete catalogues). The correlation disappears when including lower energy cosmic rays (pointing accuracy) or farther away galaxies (GZK).

This result establishes the ability to point to sources in the sky, typically within 1°, which was not a priori obvious because of uncertainties in magnetic fields met by UHECR during their journey to the Earth (typically $3\mu G$ in the disk mean $6\ 10^{17}\ eV$). A new page of astronomy has been opened as, until now, only photons could be used. It remains to be understood why such and such a galaxy, AGN or else, is a source while such and such another is not.

Not many celestial objects have large enough values of the product magnetic field × volume to be candidate sites for UHECR acceleration: as shown in Figure 14, the so-called Hillas plot [7]. Apart from magnetars which would

suffer of excessive synchrotron losses, the only possible candidates are GRBs or active galaxies already mentioned when commenting on the amount of energy which they release. In particular, SNRs are not large enough sites for UHECR acceleration. However, there exist many possible sites of large scale shocks in the Universe. Galaxy collisions are one such example [8]. Recent observations and studies of colliding galaxies and merging galaxy clusters suggest that these were common phenomena in the early denser Universe. Such collisions are now thought to have played an important role in the process of galaxy formation.

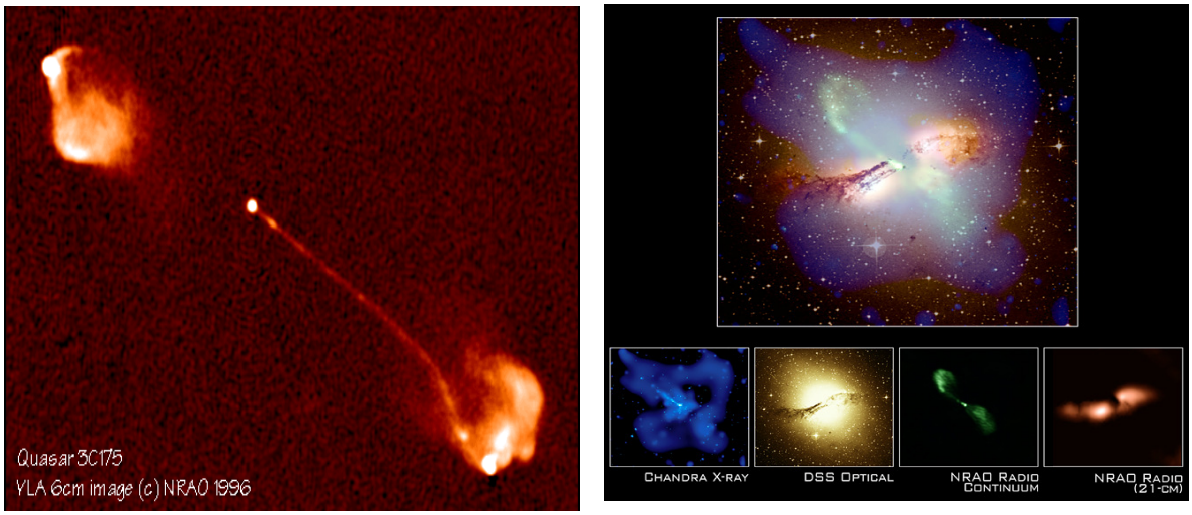

Figure 15. Left: Radio image of a quasar. Right: Centaurus A, merging of an elliptical with a smaller spiral, has an AGN in its centre (the AGN closest to us) and is the site of

They are sites of very violent events on large scales and are therefore most probably sites of large shocks. AGNs also, in particular their jets, are likely to host large size shocks and are therefore possible sites for UHECR acceleration. It seems therefore plausible that diffusive shock acceleration on such large scale shocks (Figure 15) would be the mechanism at play in the UHECR domain as it seems today to be in the galactic domain on SNRs. The observations made at the PAO in the years to come will enable identification of the preferred acceleration sites.

SUMMARY

Cosmic rays are accelerated atomic nuclei with elemental abundances as prevails in the Universe (apart from spallation reactions) but uncertainties subsist at UHECR energies; CR have a power law spectrum with index ~2.7 cut-off at ~10^{20}eV by interactions with the CMB; they contribute ~1eVcm^{-3} to the energy density of the Universe, as much as visible light, CMB or magnetic fields; they play an important role in the ISM dynamic. The Sun, wind and shocks, contributes to low energies. Most cosmic rays are of galactic origin and accelerated in the shells of young SNRs. Spectacular progress in the understanding of the

mechanism of acceleration suggests diffusive shock acceleration as a universal acceleration process. Magnetic turbulences and field amplification play an essential role. It seems possible to accommodate UHECRs in such a scenario as evidence in favour of sufficiently large scale shocks is now growing. Such shocks may be found in colliding galaxies or galaxy clusters where active galaxies are numerous. Yet, many unknowns subsist on the details and the relevant collisionless plasma physics which governs the shock region is still not well understood. One should not think that diffusive shock acceleration *must* be *the* mechanism at play. It simply is the most likely scenario in the present state of knowledge. The years to come, in particular with the PAO identifying numerous UHECR sources, will teach us a lot.

3. Extensive air showers

IDENTIFICATION OF THE PRIMARIES

When a primary cosmic ray enters the Earth atmosphere, it interacts with it and produces a large number of mesons which, in turn, interact with the atmosphere, and so on until the primary energy is exhausted in ionization losses. The result is a cascade of interactions producing what is called a shower. UHECR showers contain several billions particles at the maximum of their development and extend transversely on several square kilometres.

Their longitudinal profile (Figure 16) evolves slowly with energy, in proportion to its logarithm, while its energy content, in the form of ionization losses, is proportional to energy. Hence two standard methods to detect extensive air showers: detecting the fluorescence light produced by the shower in the atmosphere using adequate telescopes or detecting the imprint of the shower on ground by using a large array of detectors. In both cases the direction of the shower is obtained by measuring the timing of the signals detected and its energy by measuring their intensities. As the former method measures the longitudinal profile of the shower and the latter its transverse profile, they suffer very different systematic uncertainties and are highly complementary. The PAO, with 1600 ground detectors over 3000 km^2 and 24 fluorescence telescopes uses both methods simultaneously.

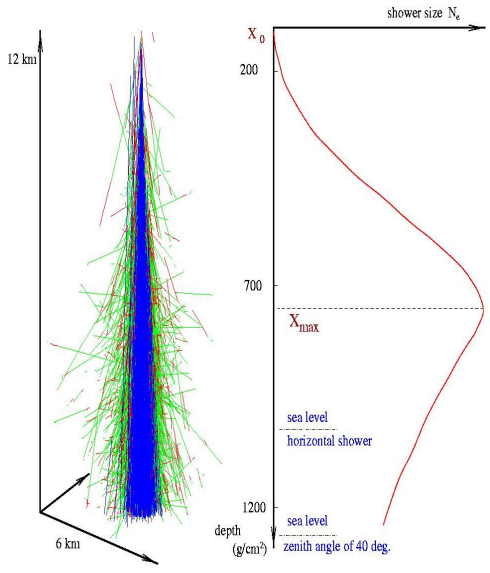

Figure 16: Longitudinal shower development.

The identification of the UHECR distribution of nuclear masses, protons or iron nuclei or whatever, is a difficult task. The depth of the maximum of the longitudinal shower profile is the main tools used for this purpose. Indeed, a shower initiated by an iron nucleus of energy E is essentially the superposition of 56 showers initiated by nucleons of energies $E/56$.

Neglecting the energy dependences of the nuclear interaction length, Λ, and of the steepness of the shower rise (both depend on energy only logarithmically) one may get a quantitative idea of the effect by using a parameterization of the shower rise of the form $((x-x_0)/a)^2$ where a is an effective scale parameter and where x_0 , the location of the first primary interaction, has a distribution of the form $\Lambda^{-1}exp(-x_0/\Lambda)$. The rise of an iron shower takes then a form:

$F(x)=\Lambda^{-1}\int((x-x_0)/a)^2exp(-x_0/\Lambda)dx_0$ (x_0 from 0 to x).

Writing $z=x_0/\Lambda$ (from 0 to x/Λ), $(a/x)^2F(x)=\int(1-\Lambda z/x)^2exp(-z)dz$

$=\int exp(-z)dz-2\Lambda/x\int zexp(-z)dz+(\Lambda/x)^2\int z^2exp(-z)dz$

$=1-exp(-x/\Lambda)+2\Lambda/x[x/\Lambda exp(-x/\Lambda)+exp(-x/\Lambda)-1]-(\Lambda/x)^2[exp(-x/\Lambda)(x/\Lambda)^2+2(x/\Lambda)exp(-x/\Lambda)+2exp(-x/\Lambda)-2]$

$=1-exp(-x/\Lambda)+2exp(-x/\Lambda)+2(\Lambda/x)[exp(-x/\Lambda)-1]-exp(-x/\Lambda)-2(\Lambda/x)exp(-x/\Lambda)-2(\Lambda^2/x^2)exp(-x/\Lambda)+2(\Lambda^2/x^2)$

$F(x)=(1/a)^2\{x^2-2\Lambda x+2\Lambda^2(1-exp(-x/\Lambda))\}$.

In the above approximation of 56 being a large number, there are no fluctuations from one iron shower to the next while there are important fluctuations (with scale Λ) from one proton shower to the next. Moreover, the typical proton shower starts much later than the iron shower. Taking $x_0=\Lambda$ for the proton shower, $F^{proton}(\Lambda)=0$ and $F^{iron}(\Lambda)=0.264(\Lambda/a)^2$, a value reached by F^{proton} at $x=1.514\Lambda$.

Figure 17

Figure 17: Energy dependence of the depth at which showers reach their maximum.

Figure 17 illustrates the present experimental situation. The value X_{max} of the atmospheric depth traversed when the shower reaches its maximum is plotted as a function of the logarithm of the shower energy. The measured values fall in between the proton and iron predictions of shower development simulations. On another hand, the strong correlation observed between UHECRs and AGNs suggests that most UHECR are protons. These possibly conflicting results call for a deeper understanding of the data, in particular of possible systematic errors attached to the measurements. In this context, the influence of LPM suppression, which delays the start of electromagnetic showers, is of utmost relevance. Although LPM suppression does not directly affect the location of the

first interaction (defined by Λ) it does affect the development of the electromagnetic showers induced by the decay photons of the many π^0 mesons produced in this first interaction (on which a depends).

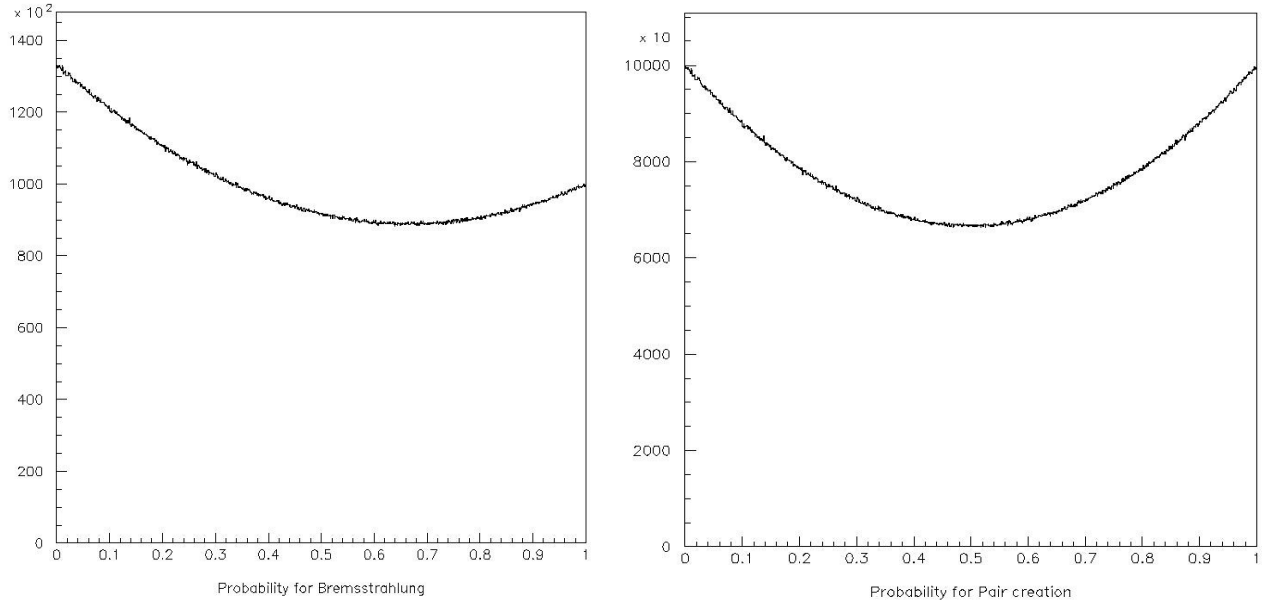

Figure 18. Right: Differential pair creation probability per unit of radiation length as a function of the fractional energy taken by the electron. Left: Differential bremsstrahlung probability per unit of radiation length and per $d\eta/\eta$ as a function of the fractional energy taken away by the photon. The ordinates are multiplied by 10^5.

LONGITUDINAL DEVELOPMENT OF ELECTROMAGNETIC SHOWERS

Electromagnetic showers may be initiated by an electron (or positron: in what follows electron is to be understood as electron or positron unless specified otherwise) or a photon. A code, available at VATLY, simulating their longitudinal development has been used for the study of the LPM suppression. It is briefly described below.

Particle types other than electrons, positrons and photons that may be created in the cascade (such as $\mu^+\mu^-$ pairs from photon conversion) are ignored. Moreover the only processes that are considered are pair creation in the case of photons and bremsstrahlung in the case of electrons. Namely other effects, such as Compton scattering, photoelectric effect, etc… are ignored.

To an excellent approximation, the probability d^2P for a photon of energy E to convert in a medium of interaction length X_0 (in g/cm^2) over a thickness $x=X_0\,dt$ (t has no dimension, x is measured in g/cm^2), into a pair having an electron of energy in the interval $[\eta, \eta+d\eta]$ (the positron energy being in the interval $[E-\eta, E-\eta-d\eta]$) is

$$d^2P=\{1-4/3\ \eta/E\ (1-\eta/E)\}d\eta/E\ dt \qquad (1)$$

The dependence of $Ed^2P/d\eta dt$ on η/E is displayed in Figure 18 (right). It has a parabolic shape with a minimum of *2/3* corresponding to the symmetric case (electron and positron having equal energies). It is symmetric in the exchange of the electron and positron (η/E becoming $1-\eta/E$). Note that integrating over η/E gives

$$dP/dt = [u - 2/3\ u^2 + 4/9\ u^3]^1_0 = 7/9 \qquad (2)$$

This means that the distribution of photons as a function of the thickness traversed, $x=tX_0$, is an exponential of the form $exp(-7/9t)$: the characteristic length over which the number of photons decreases by a factor *1/e* is $9/7\ X_0$. X_0 is called the radiation length (the reason for this name will become clear when we consider bremsstrahlung).

In the case of an incident electron of energy E, the probability d^2P to bremsstrahl, over a distance $dx=X_0dt$, a photon having an energy in the interval $[\eta, \eta+d\eta]$ is, to a good approximation,

$$d^2P = \{4/3 - 4/3\ \eta/E + (\eta/E)^2\}\ d\eta/\eta\ dt \qquad (3)$$

It is illustrated in Figure 18 (left) where $d^2P/(dt\ d\eta/\eta)$ is plotted against η/E. It reaches a minimum at 8/9 for η/E =2/3 while being unity when $\eta=E$ and being 4/3 when $\eta=0$. The total energy bremsstrahled per interval dt is

$$\int \eta\ d^2P = \{4/3\ E - 4/3\ E/2 + E/3\}\ dt = E\ dt.$$

The remaining energy has therefore an exponential dependence over the thickness $x=tX_0$ traversed of the form e^{-t}. It falls by a factor *1/e* after each radiation length traversed. This justifies the name "radiation length" given to X_0.

However, things are more subtle when considering the number of photons bremsstrahled, which, according to the expression obeyed by d^2P, is infinite. Indeed, an infinite number of zero energy photons are bremsstrahled. It is therefore necessary to introduce a cut-off ε below which photons are ignored. Then, the number of bremsstrahled photons having energy in excess of ε is obtained by integration over η between ε and E:

$$dN = \{4/3 \ln E/\varepsilon - 5/6 + 4/3\ \varepsilon/E - 1/2\ (\varepsilon/E)^2\}dt \qquad (4)$$

The multiplication of particles in the cascade is counteracted by the energy losses which they suffer. Here ionization losses are described very simply by the Bethe Bloch formula

$$dE/dx = -KZz^2/\beta^2\ [\ln(2mc^2\beta^2\gamma^2/I) - \beta^2 - \delta/2] \qquad (5)$$

where the energy loss dE in a slice dx (in g/cm^2) is given as a function of the particle velocity βc, c being the velocity of light; γ is the relativistic parameter, $(\beta\gamma)^2 = \gamma^2 - 1$; z and Z are the charges of the incident particle and target nucleus respectively; I is the ionization potential (which is of the order of $16\ Z^{0.9}\ eV$); δ is the density effect correction responsible for the slow rise (so-called relativistic rise) of the differential energy loss at high energies; K is a constant. In practice, as E is always larger than three electron masses (see below) the relativistic approximation below is used (Figure 19)

$$dE/dx=(dE/dx|_{min}/11MeVg^{-1}cm^2)\{(1+(m/E)^2)(ln(E/m)+6)+3.2\} \quad (6)$$

Moreover, the slowing down at the end of the Bragg curve, just before stopping, is replaced by a simple cutoff: any particle having energy below some threshold (here set at 1.5 MeV) is no longer considered. This cut-off applies to both electrons and photons and their energy is added to the shower.

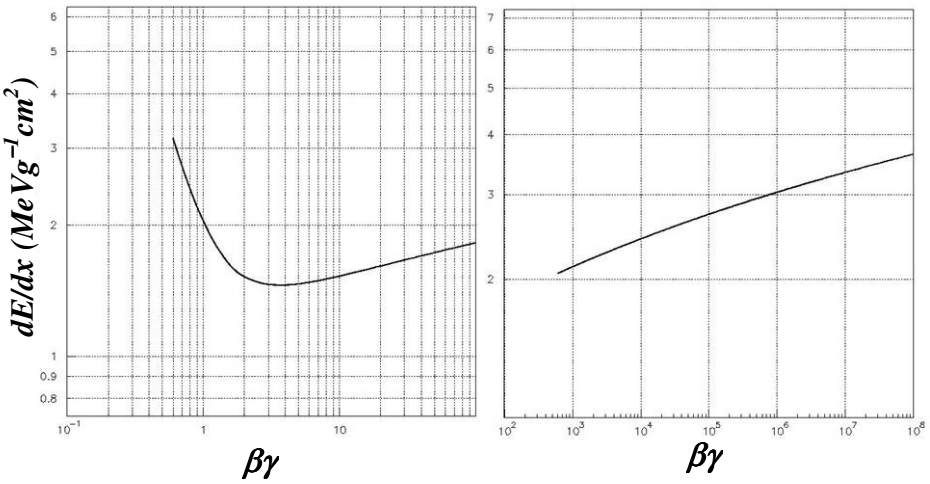

Figure 19: Differential ionization energy loss in iron.

A few typical shower development profiles for a 30 GeV electron incident on iron are shown in Figure 20. Large fluctuations are observed from shower to shower.

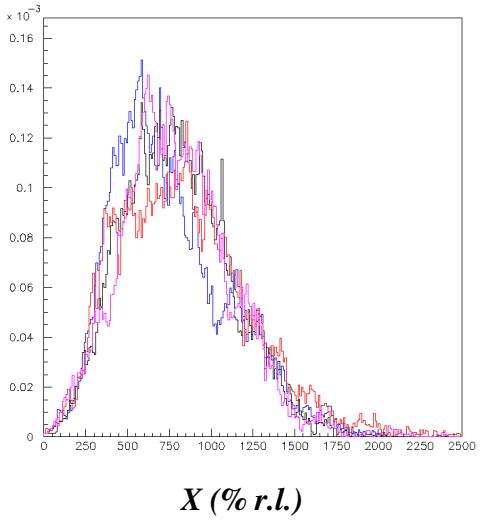

Figure 20: Some typical shower development profiles for a 30 GeV electron incident on iron. The depth *X* is measured in percent of a radiation length.

GAISSER HILLAS PROFILES

The use of the above code at UHECR energies is not practicable because of the too large number of secondaries being produced. Many codes use statistical tricks to overcome this difficulty (sampling, thinning, etc.). Here, a different approach is adopted: one proceeds by iterations to define parameterizations of the shower profiles as a function of energy. These parameterizations describe both the mean profile and its fluctuations from shower to shower; namely, both the mean and rms values of the relevant parameters are evaluated as a function of energy.

To this aim, longitudinal shower profiles are described using the standard Gaisser Hillas function

$$S = S_{\max}\left(\frac{X - X_0}{X_{\max} - X_0}\right)^{\frac{X_{\max} - X_0}{W}} e^{\frac{X_{\max} - X}{W}} \qquad (7)$$

where S is the density of charged particles at depth X in the medium. In practice, SdX may be the sum of the charged particle track lengths in the transverse shower slice between X and $X+dX$, or the energy ionization loss in that same slice, or the amount of Cherenkov light produced in that same slice. At high energies, all three distributions are expected to have similar shapes, which can be described by Gaisser Hillas profiles. The depth variable X is measured in g/cm^2 with dX being the product of the local density by the thickness of the slice. In a solid medium, such as the case of iron, which we take as an example in what follows, X simply scales with distance while in the case of air showers the dependence of density on altitude trivially distorts X with respect to distances.

The quantity X_0 defines where the shower, understood as its charged particle components, starts developing. In particular, in the case of a photon, it starts at the location of the first pair creation while in the case of an electron it essentially starts at $X_0=0$. Obviously, once started, the shower develops independently from X_0 and S depends explicitly on $X–X_0$ only.

Reduced variables are introduced taking S_{max} and $X_{max}–X_0$ as units and shifting the origin of abscissa by X_0 : $\eta=S/S_{max}$ and $\xi=(X–X_0)/(X_{max}–X_0)$.

The reduced profile then reads $\eta=\{\xi exp(1–\xi)\}^{\delta}$ and depends on a single parameter $\delta=(X_{max}–X_0)/W$. Equivalently, $ln\eta=\delta(ln\xi+1–\xi)$.

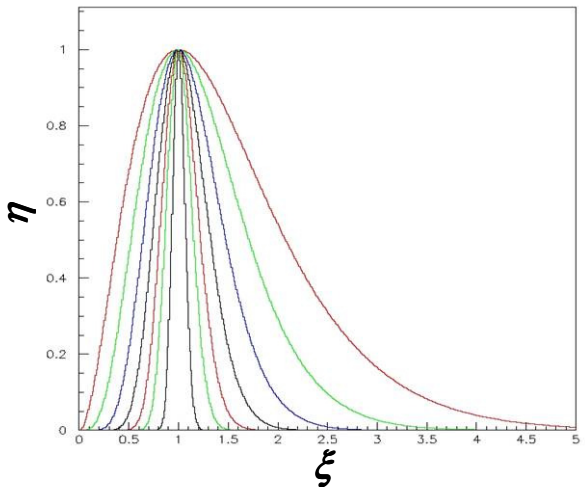

Figure 21. Reduced profiles for different values of the parameter δ (2, 4, 8, 16, 32, 64, 256)

The reduced profile starts at 0 at the origin as ξ^{δ} and approaches 0 again when $\xi \to \infty$. Differentiating gives $d\eta/d\xi = \eta\delta(1/\xi - 1)$ which cancels for $\xi = 1$ where η reaches its maximum value, *1*, independently from δ. Therefore, the real profile reaches its maximum value S_{max} at $X = X_{max}$ which justifies their names.

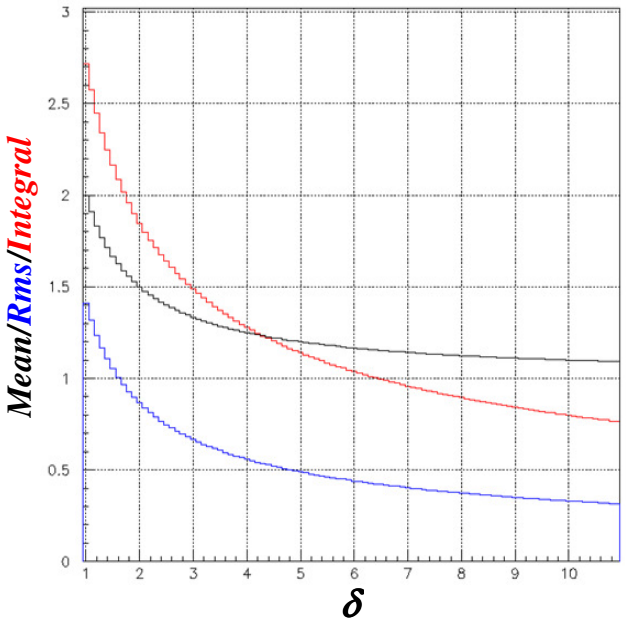

Figure 22. Dependence on δ of the mean value (black), rms value (blue) and integral (red) of the reduced profile.

The second derivative, $d^2\eta/d\xi^2 = \eta\delta^2(1/\xi - 1)^2 - \eta\delta/\xi^2$ cancels for $\delta(1/\xi - 1)^2 = 1/\xi^2$ or $\xi = 1 \pm 1/\sqrt{\delta}$. While the turning points are equidistant from $\xi = 1$ the profile is not at all symmetric around this value. As illustrated in Figure 21 it is significantly skewed, the more the larger δ. For $\delta > 1$ the profile starts tangent to the ξ axis, for $\delta < 1$ it starts tangent to the η axis and for $\delta = 1$ it starts on the bisector. At high enough energies δ is always > 1. Analytic expressions of the mean, rms and integral values are given in Table 1 below, both for the reduced profile and the real one. Figure 23 illustrates their dependence on δ.

Table 1. Gaisser Hillas parameters.

Parameter	Reduced profile	Real profile
Mean value	$1 + 1/\delta$	$X_0 + (X_{max} - X_0)(1 + W/(X_{max} - X_0))$
Rms value	$(\sqrt{(1+\delta)})/\delta$	$\sqrt{((W + X_{max} - X_0)W)}$
Integral	$J(\delta) = e^{\delta}\Gamma(\delta+1)/\delta^{\delta+1}$	$S_{max}(X_{max} - X_0)J((X_{max} - X_0)/W)$

The real profile depends on four parameters. The knowledge of its gross features, i.e. its mean value $<X>$, rms value, $Rms(X)$ and integral Σ is not sufficient to fix them. A fourth quantity, such as a higher order moment, skewness, etc, must also be known. The knowledge of $<X>$ and of $Rms(X)$ fixes W and $(X_{max}–X_0)$. Conversely, it fixes X_0 once $(X_{max}–X_0)$ is known, or fixes $(X_{max}–X_0)$ once X_0 is known. The knowledge of Σ then fixes S_{max}. Eliminating X_0 or $(X_{max}–X_0)$ from the expression of $<X>$ and $Rms(X)$ makes the correlation that needs to be lifted explicit: $Rms(X) = \sqrt{\{W(W+ X_{max}–X_0)\}}$ or $= \sqrt{\{W(<X> – X_0)\}}$.

PARAMETERIZED SHOWER PROFILES

X_0 is evaluated first directly as the depth at which the profile starts to rise and, in a second step, X_{max} , S_{max} and W are calculated by using the expressions in Table 1 to reproduce the experimental values of $<X>$, $Rms(X)$ and $\Sigma = \int SdX$.

Explicitly,

$$\delta = \{(<X>–X_0)/ Rms(X)\}^2 - 1 \qquad X_{max} = X_0+(<X>–X_0)\delta/(\delta+1)$$
$$S_{max} = \Sigma\, \delta^{\delta+1} exp(-\delta)/\Gamma(\delta+1)/(X_{max}-X_0) \qquad W = (X_{max}-X_0)/\delta \tag{8}$$

Care has been taken to find combinations of the above parameters having essentially no correlation among them. Accordingly, the following set of parameters was retained to define the showers:

X_0 , $<X>–X_0$, $\rho=Rms(X)/(<X>–X_0)$ and Σ.

Both $<X>–X_0$ and ρ are found to depend on the logarithm of the energy, the former increasing linearly while the latter decreases. The rms value of the former is constant within errors while that of the latter decreases slowly with the logarithm of the energy. The difference between electron and photon showers is essentially due to the difference in X_0. Once a photon is converted the shower develops as the superposition of two lower energy electron showers. Indeed, the value of $<X>–X_0$ is accordingly slightly lower for a photon than for an electron of the same energy.

The extrapolation to higher energies proceeds in steps of a factor of 2 in energy E_0: 30 GeV, 60 GeV, 120 GeV, and so on up to 10^{12} GeV. The generation of the shower is done as described earlier except that whenever one meets an electron or photon having an energy smaller than $E_0/2$ one stops the shower development procedure and replaces it by a sub-shower of the proper energy. Namely one chooses a Gaisser-Hillas profile with parameters corresponding to the desired energy. Each parameter is chosen at random with a Gaussian distribution having the proper mean and rms values.

The energy dependence of the mean and rms values of the distributions of $<X>–X_0$ and ρ are illustrated in Figure 23. While $<X>–X_0$ increases linearly with the logarithm of the energy, $<X>–X_0=A+Blog_{10}(E/10^{10}MeV)$, the variable $W=<\rho>^2<<X>–X_0>$ is found to be constant and takes the value 1.51±0.01 and 1.53±0.03 radiation lengths for electrons and photons respectively. The values taken by the parameters A and B (measured in radiation lengths) are respectively

19.6, 2.31 for photons and 20.1, 2.31 for electrons. Figure 24 shows the values of $b=1/W$ found for various elements at low energy by a sophisticated shower simulation code [11]. The value of W found by the present approach corresponds to $b\sim1/1.52=0.66$, namely the value obtained for light elements such as carbon. This is appropriate when using our code for extensive air showers. Note that in the present approach, the only parameter differentiating between different elements is the value of the Bethe Bloch ionization losses as long as results are expressed in units of radiation lengths.

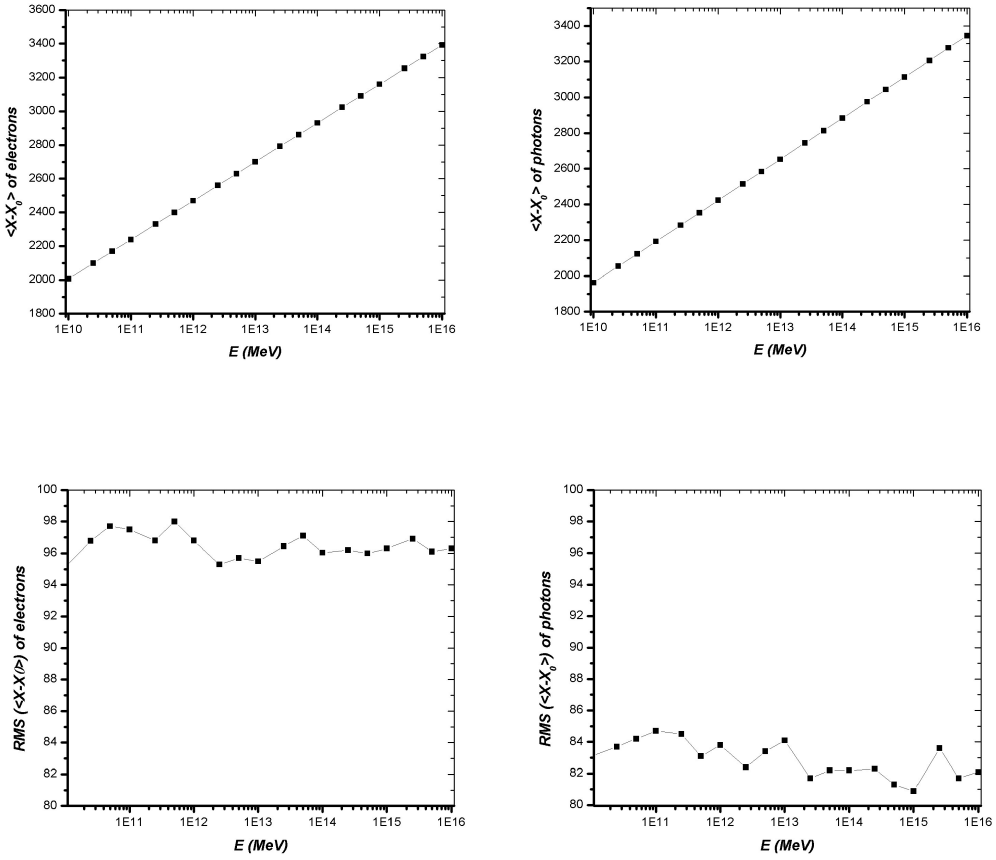

Figure 23 a: Distributions of the mean values (upper panels) and rms values (lower panels) of $<X-X_0>$ for electrons (left panels) and photons (right panels) respectively.

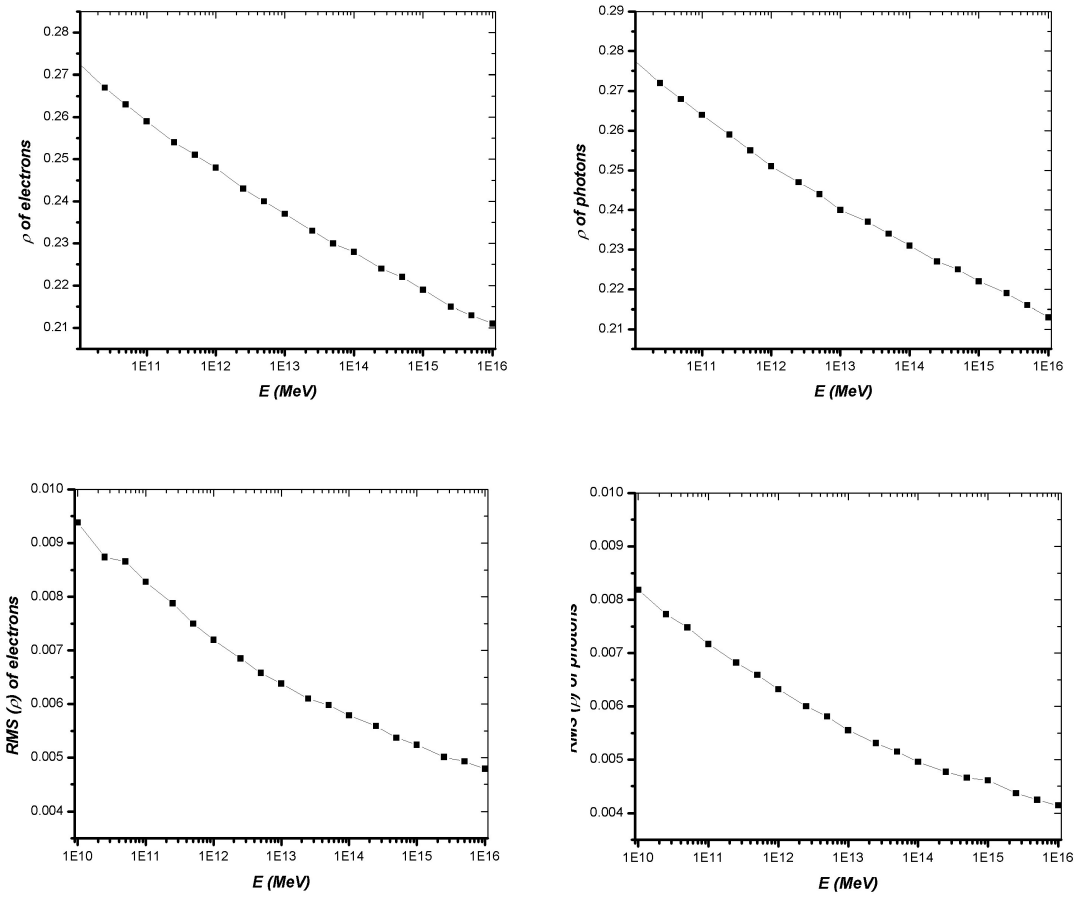

Figure 23 b: Distributions of the mean values (upper panels) and rms values (lower panels) of ρ for electrons (left panels) and photons (right panels) respectively.

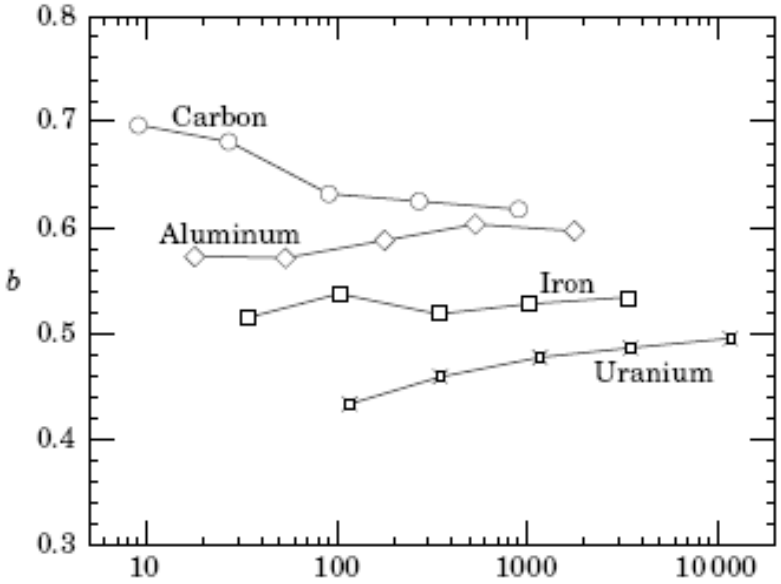

Figure 24: Distribution of *b=1/w* as calculated using the code EGGS for various elements. The abscissa is the ratio of the energy to the critical energy. Exact scaling implies that *w* is independent from energy.

4. The LPM effect

LPM SUPPRESSION OF BREMSSTRAHLUNG AND PAIR CREATION

The electromagnetic portion of high energy air showers is governed by bremsstrahlung and pair production. Although the standard Bethe Heitler formulae for these processes have been around for over 60 years, in many situations, these formulae can be very wrong. The medium in which the bremsstrahlung or pair creation occurs can drastically suppress the cross sections, hence increasing the effective radiation length, lengthening the showers, and moving the position of the shower maximum deeper into the atmosphere, therefore affecting measurements of the composition of the highest energy cosmic rays.

Suppression mechanisms for bremsstrahlung and pair production are possible because of the unusual kinematics in these processes. For ultrarelativistic particles, the momentum transfer between the radiating electron or converting photon and the target nucleus is very small, especially in the longitudinal direction. For bremsstrahlung, when the electron energy $E >> m$, transverse momenta can be neglected and the longitudinal momentum transfer is:

$$q_L = p_e - p'_e - k \tag{9}$$

$$= \sqrt{(E^2 - m^2)} - \sqrt{\{(E-k)^2 - m^2\}} - k$$

$$= m^2 k / \{2E(E-k)\} \tag{10}$$

where p_e and p'_e are the electron momenta before and after the interaction respectively, k is the photon energy, m is the electron mass and $\gamma = E/m$.

For ultrarelativistic electrons, q_L can be very small. For example, for a 10^{18}eV electron emitting a 10^{17}eV photon, $q_L = 10^{-8} eV$. Because q_L is so small, by the uncertainty principle the emission must take place over a long distance, known as the formation length:

$$l_{f0} = \hbar / q_L = 2\hbar E(E - k)/(m^2 k) \tag{11}$$

For the above example, l_{f0} is 20 metres; for a 10^{15} eV photon from the same electron, l_{f0} rises to 2 km. This distance is the distance required for the electron and photon to separate and to become distinct particles. It is also the path length over which the emission amplitude adds coherently to produce the emission probability. If something happens to the electron or nascent photon in the formation zone, the coherence can be disrupted; it may then reduce the effective formation length and, hence, the emission probability. Even weak forces, acting over a long formation length, can be strong enough to destroy the coherence required for emission.

Multiple scattering can cause disruption by changing the electron trajectory. If, taken over l_{f0}, the electron multiple scatters by an angle larger than the typical bremsstrahlung emission angle $1/\gamma$, then emission can be suppressed [1]. The reduction can be calculated by considering the effect multiple scattering has on q_L; as the electron changes direction, its forward velocity is reduced, producing a

change in q_L. This can be modelled by dividing the multiple scattering evenly between p_e and p'_e.

Then,

$$q_L = \sqrt{\{(E\cos\theta_{MS/2})^2 - m^2\}} - \sqrt{\{(E-k)\cos\theta_{MS/2})^2 - m^2\}} - k \qquad (12)$$

where $\theta_{MS/2}$ is the multiple scattering in half the formation length, $E_s/E\sqrt{(l_f/2X_0)}$, where $E_s = m\sqrt{(4\pi\alpha)} = 21\ MeV$, and X_0 is the radiation length. Scattering after the interaction is for electron energy $E-k$. This leads to a quadratic in l_f:

$$l_f = 2\hbar E(E-k)/\{km^2(1+[E_s^2 l_f]/[m^2 X_0])\} = l_{f0}\{1+(E_s^2 l_f)/(m^2 X_0)\}^{-1}. \qquad (13)$$

If multiple scattering is small, this reduces to Eq. (11). When multiple scattering dominates

$$l_f = \sqrt{\{2\hbar E(E-k)X_0/(E_s^2 k)\}} = l_{f0}\sqrt{\{(kE_{LPM})/(E(E-k)\}}\ . \qquad (14)$$

where E_{LPM} is a material dependent constant, given by

$E_{LPM} = m^4 X_0/(2\hbar E^2) \approx 3.85\ TeV/cm\ X_0$. For lead, $E_{LPM} = 2.2\ TeV$, while for water $E_{LPM} = 139\ TeV$ and for sea level air $E_{LPM} = 1.17\ 10^{17} eV$.

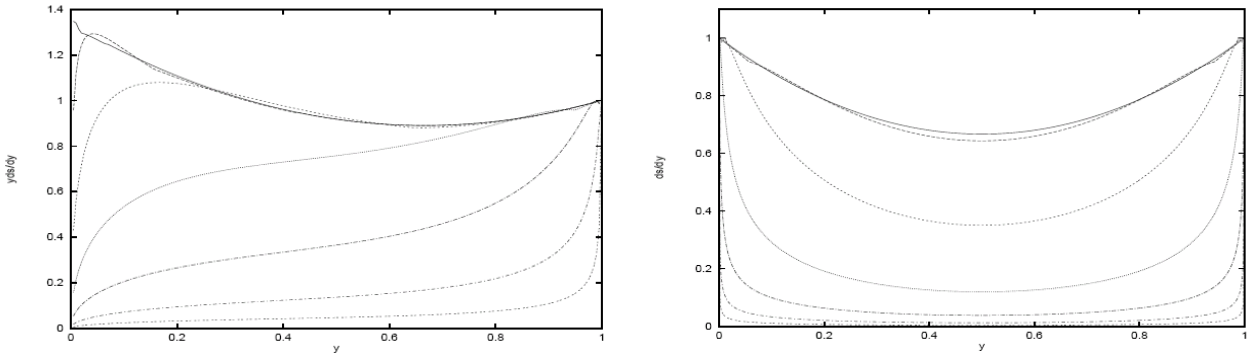

Figure 25: Same as Figure 18. The dashed curves illustrate the effect of LPM suppression. They have been calculated in energy steps of a factor of 10 starting at 100GeV for bremsstrahlung (left) and at 10TeV for pair creation (right). The calculation is made for lead where E_{LPM}=2.2TeV.

Since the formation length is the maximum distance over which the bremsstrahlung amplitude add coherently, the bremsstrahlung amplitude is proportional to the formation length, so the suppression factor is

$$S = (d\sigma/dk)/(d\sigma_{BH}/dk) = l_f/l_{f0} = \sqrt{(kE_{LPM}/(E(E-k))} \qquad (15)$$

and the $dN/dk \sim 1/k$ found by Bethe and Heitler changes to $dN/dk \sim 1/\sqrt{k}$.

A similar effect occurs for pair creation, where the produced electron and positron can multiple scatter. The two effects are closely related and this relationship can be used to relate the bremsstrahlung and pair creation formation lengths and cross sections. For pair production

$$l_{f0} = 2\hbar E(k-E)/m^2 k \qquad (8)$$

the corresponding suppression is

$$S = \sqrt{(kE_{LPM}/E(k-E)}\ . \qquad (9)$$

Migdal [3] has performed a more elaborate calculation of the effect and his results are shown in Figure 25. Fig. 25 (left) shows the LPM bremsstrahlung suppression of $yd\sigma/dy$ $(y = k/E)$ for electrons in a lead target. The 10 GeV electron curve is very close to the Bethe-Heitler prediction; in the absence of suppression, this curve would hold for all electron energies. As the electron energy rises, emission drops. At the highest electron energies, photons with $k \sim E$ are almost completely suppressed. Fig. 25 (right) shows how the pair creation cross section is reduced. Compared with bremsstrahlung, pair creation suppression sets in at higher energies. Symmetric pairs are suppressed the most; in the extremely high energy limit, one of the produced electrons takes almost all of the photon energy. So, where the LPM effect is extremely strong, an electromagnetic shower becomes a succession of interactions where an electron emits a bremsstrahlung photon that takes almost all of the electron energy, followed by a very asymmetric pair conversion, producing an electron or positron with almost all of the energy of the initial lepton. It is interesting to note that in such a process a very high energy electron has a 50% chance to turn into a very high energy positron, making offence to common sense.

EXPERIMENTAL EVIDENCE

The LPM effect was studied experimentally at SLAC using 8 and 25 GeV electrons on thin (0.1 % to 6% of X_0) targets of materials ranging from carbon to gold [10]. Fig. 26 shows the experimental set-up. The beam, 120 pulses per second, each containing one electron on average, was bent horizontally by 39 mrad after having crossed the target and directed on a spectrometer made of wire chamber planes followed by a lead glass array. The bremsstrahlung photons were detected in a high resolution BGO array, 50 m downstream the target. To minimize background, the bent electron path and the photon flight path were evacuated. Data were recorded at each pulse and events having a single electron in the lead glass array and obeying the bremsstrahlung kinematics were recorded. The photon energy was measured with a typical 4% energy systematic uncertainty. The data are of excellent quality. Figure 27 shows data recorded with a 25 GeV incident beam on gold targets of respectively 6% and 0.7% X_0 thicknesses. They are compared with both the Bethe Heitler (no LPM suppression) and the Migdal predictions. The important deviation observed on the thinner target data is easily explained as an edge effect: when the

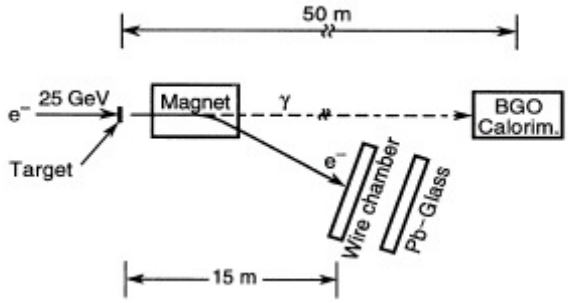

Figure 26: SLAC experimental set-up

first bremsstrahlung takes place close to the target end, i.e. at a distance from its downstream edge small with respect to the formation length, the effect of multiple scattering is obviously reduced and the LPM suppression is less than for a thick target. Indeed, subtracting the *0.7% X_0* data from the *6% X_0* data achieves an excellent match between Migdal's predictions and experiment. Moreover, data recorded on a very thin (*0.1% X_0*) target show essentially no suppression, as expected. In summary, the Migdal theory of the LPM effect is found to accurately describe experimental data.

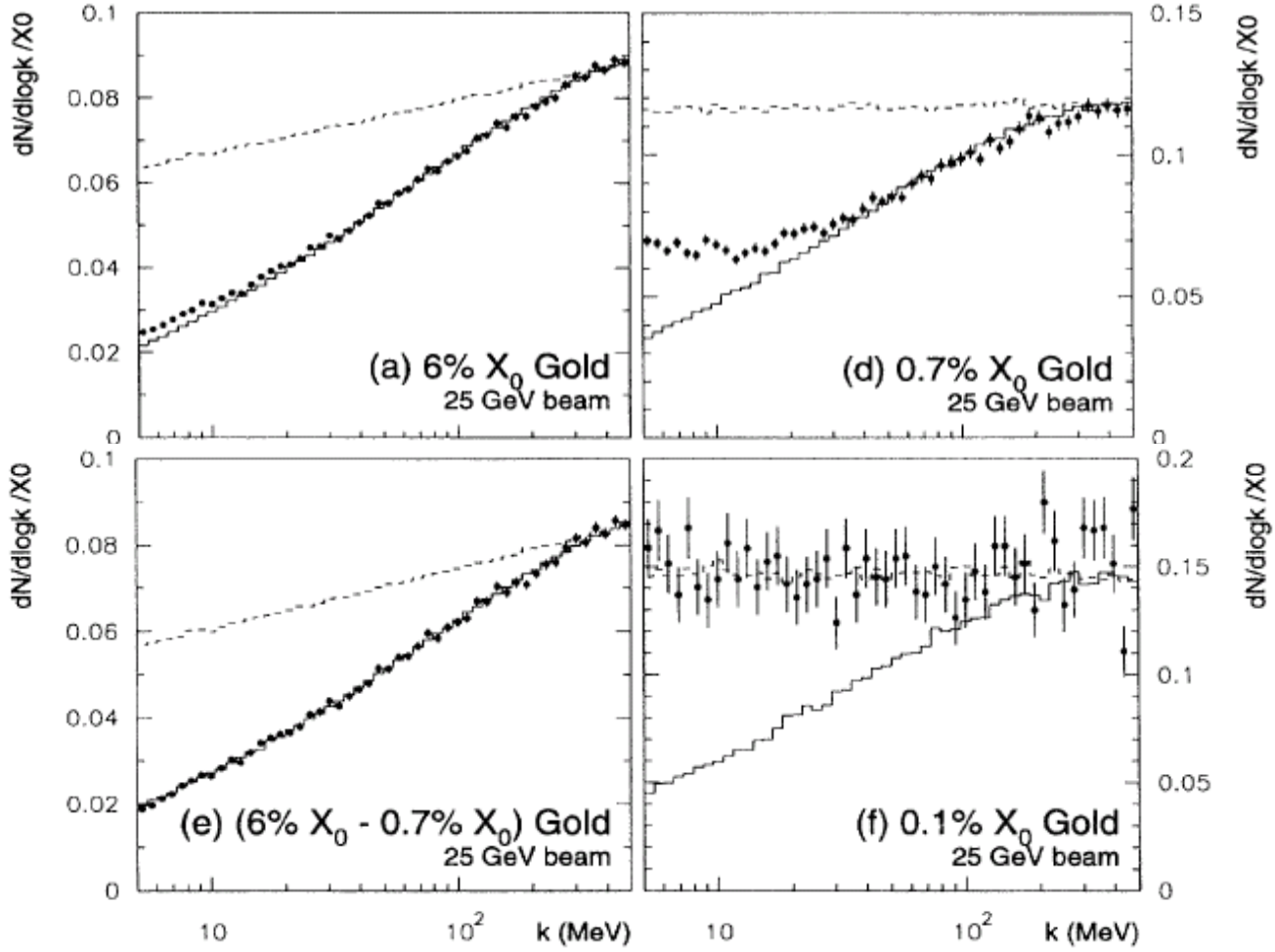

Figure 27: Dependence of $dN/[d(logk)/X_0]$, where N is the number of events per photon energy bin per incident electron. The photon energy scale is logarithmic with 25 bins per decade, so each bin has a width $\Delta k \sim 0.0964\ k$. The dashed and full lines are Bethe Heitler and Migdal respective predictions.

SUMMARY

The effective increase in radiation length is shown in Fig. 28; it shows how the area under the curves in Fig. 25 drops as the incident particle energy rises. For bremsstrahlung, energy loss is halved for electrons with $E=22E_{LPM}$, while the pair

production cross section is halved for $k=100E_{LPM}$. The initial part of a shower will consist almost entirely of a few high energy particles, without an accompanying "fuzz" of lower energy particles. The initial shower development depends on a much smaller number of interactions. For example, a 25 GeV electron in sea level air will emit about 14 bremsstrahlung photons per X_0, while a 10^{17} eV electron will emit only 3. Pair production is similar; the pairs become increasingly asymmetric.

The higher energy lepton from a 25 GeV photon pair conversion takes an average of 75% of k; for a 10^{19} eV photon, the average is more than 90%. Because of this, shower to shower fluctuations become much larger. In the limit $E \sim E_{LPM}$, the initial part of an air shower becomes a succession of asymmetric pair production, where the higher energy of the pair loses most of it's energy to a single bremsstrahlung photon, re-starting the process.

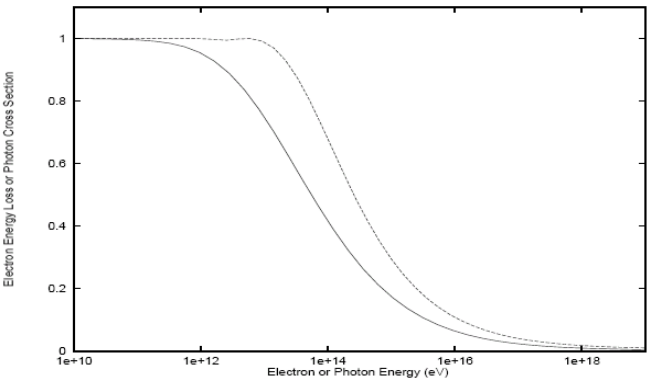

Figure 28: LPM suppression in electron energy loss, $\int_0^E$(dN/dk)kdk (solid line) and in the photon conversion cross section (dashed line) for lead.

Air showers studies are complicated by the fact that density, and hence E_{LPM}, depend on altitude. Pressure decreases exponentially with altitude, with scale height 8.7 km. For showers, it is convenient to work with column depth measured in g/cm^2 and $E_{LPM} = 1.17\ 10^{17} eV(A_0/A)$, where A is the column depth and A_0 is ground level, $1030\ g/cm^2$. E_{LPM} is $2.25\ EeV$ at $36\ g/cm^2$ ($1\ X_0$) depth, and $1\ EeV$ at $90\ g/cm^2$ (1 hadronic interaction length, Λ). A central hadronic collision will produce a shower of several hundred pions; the neutral pions will decay to photons. The highest energy π^0 will have rapidity near to the incoming proton, and their decay photons will have energies around $2\times10^{19} eV$. Many diffractive processes, such as Δ production can produce photons with similar energies. Overall, photons from central interaction will have an average energy of about 2 10^{17} eV. However, as the bulk of the produced π^0's are of much lower energies, the LPM suppression effect is strongly diluted.

As the pressure depends on altitude, it is no longer possible to express the shower development as exclusive function of the radiation. The same comment applies to the decay paths of $\pi^0 s$ and $\pi^{\pm} s$. A realistic shower development simulation will therefore depend on zenith angle. However, to keep the present calculation as simple as possible, we restrict its scope to vertical showers and neglect the π^0 decay path, which is $\sim 20\ cm/PeV$.

5. Simulation of LPM suppressed showers; the main results

In order to study the effect of LPM suppression on extensive air showers, we proceed in two successive steps. In a first step we look at the effect of increasing the effective radiation length as displayed in Figure 28. In a second step we include the effect of the different energy sharing between the two particles in the final state as displayed in Figure 25.

Let F_e and F_γ be the suppression functions displayed in Figure 28 for lead where $E_{LPM}=2.2\ TeV$. For air, at altitude z (in km), $E_{LPM} = 1.17\ 10^{17} eV(A_0/A)$ and $A=A_0 exp(-z/8.7)$. Hence $E_{LPM} = 1.17\ 10^{17} eV\ exp(z/8.7)$. Knowing z, the suppression is $F\{E\times(2.2/1.17)\times 10^{-5}\times exp(-z/8.7)\}$. Therefore, the shower development simulation proceeds as before and at step n, after having crossed n percent of a radiation length (X_0), one calculates z as $1030\ exp(-z/8.7)= n\ 36/100$ where one has used $A_0=1030\ g/cm^2$ and $X_0=36\ g/cm^2$. Hence $z=8.7ln(103000/[36n])$. Then the suppression factors are calculated as

$F\{E\times(2.2/1.17)\times 10^{-5}\times exp(-z/8.7)\}.=F\{E\times(2.2/1.17)\times 10^{-5}\times 36\ n/103\ 000\}$

$=F\{6.6En10^{-9}\}$. When deciding whether there is bremsstrahlung or whether there is pair creation, it is therefore sufficient to multiply the probabilities by the corresponding values of F_e and F_γ.

The results are displayed in Figures 29 to 31 below (red curves). The effect of LPM suppression becomes significant above 10^{19}eV. By 10^{21}eV, the increase of the average shower length reaches 16% for photons and 24% for electrons. However, in the photon case, the shower starts also significantly later as the first conversion occurs with a lower probability (directly measured by F_γ). Globally, the effect is therefore of the order of 24% for both electrons and photons. Much more spectacular is the increase of the size of the shower to shower fluctuations. The rms values of $X–X_0$ are multiplied by a factor 12 at 10^{21}eV. A similar behaviour is found in the case of ρ, the mean value of which increases by 22% at 10^{21}eV while its rms value is again multiplied by a factor 10. The W parameter has increased by 85% by 10^{21}eV, with comparable contributions from the increases of $X–X_0$ and of ρ^2.

We now include the effect of LPM suppression on the energy sharing in the final state (Figure 25); the results are shown in green in Figures 29 to 31.

In extensive air showers, the seeds of electromagnetic showers are photons from the decay of neutral pions. As these neutral pions are produced with a high multiplicity in the primary hadronic interaction, only a very few of them have very high energies and the effect of LPM suppression is accordingly diluted by a large factor. As the GZK cut-off limits the primary energies to ~10^{21}eV, the effect of LPM suppression will therefore be small on the mean shower length and width. However, it may produce significant effects on the shower to shower fluctuations. This will complicate the use of shower to shower fluctuations as a measure of the mass of the primary.

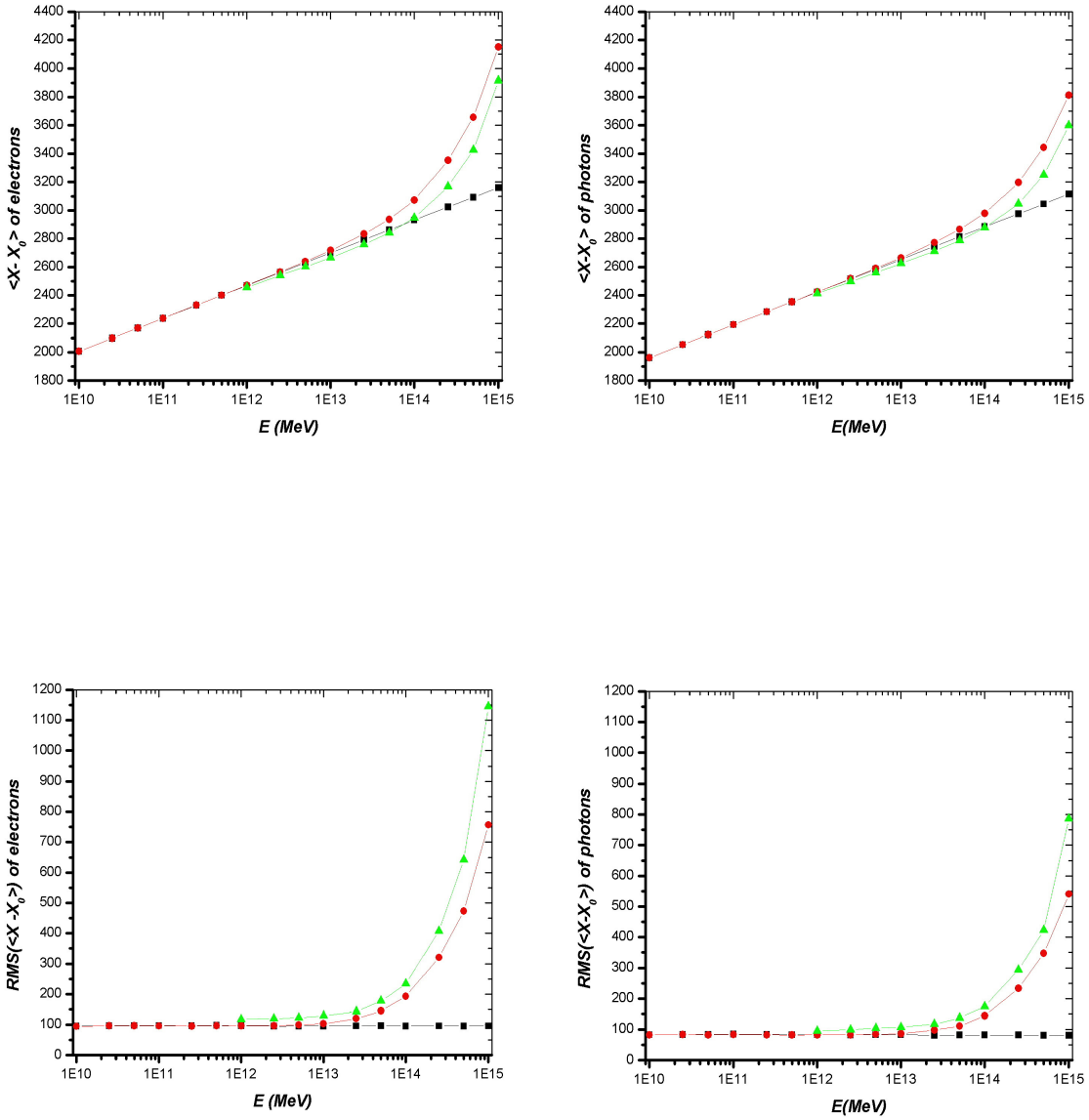

Figure 29a: Distributions of the mean values (upper panels) and rms values (lower panels) of $\langle X\text{-}X_0 \rangle$ with LPM suppression (green) compared with no LPM suppression (black) for electrons (left panels) and for photons (right panels). The red curves treat LPM suppression globally but ignore its effect on fractional energy sharing.

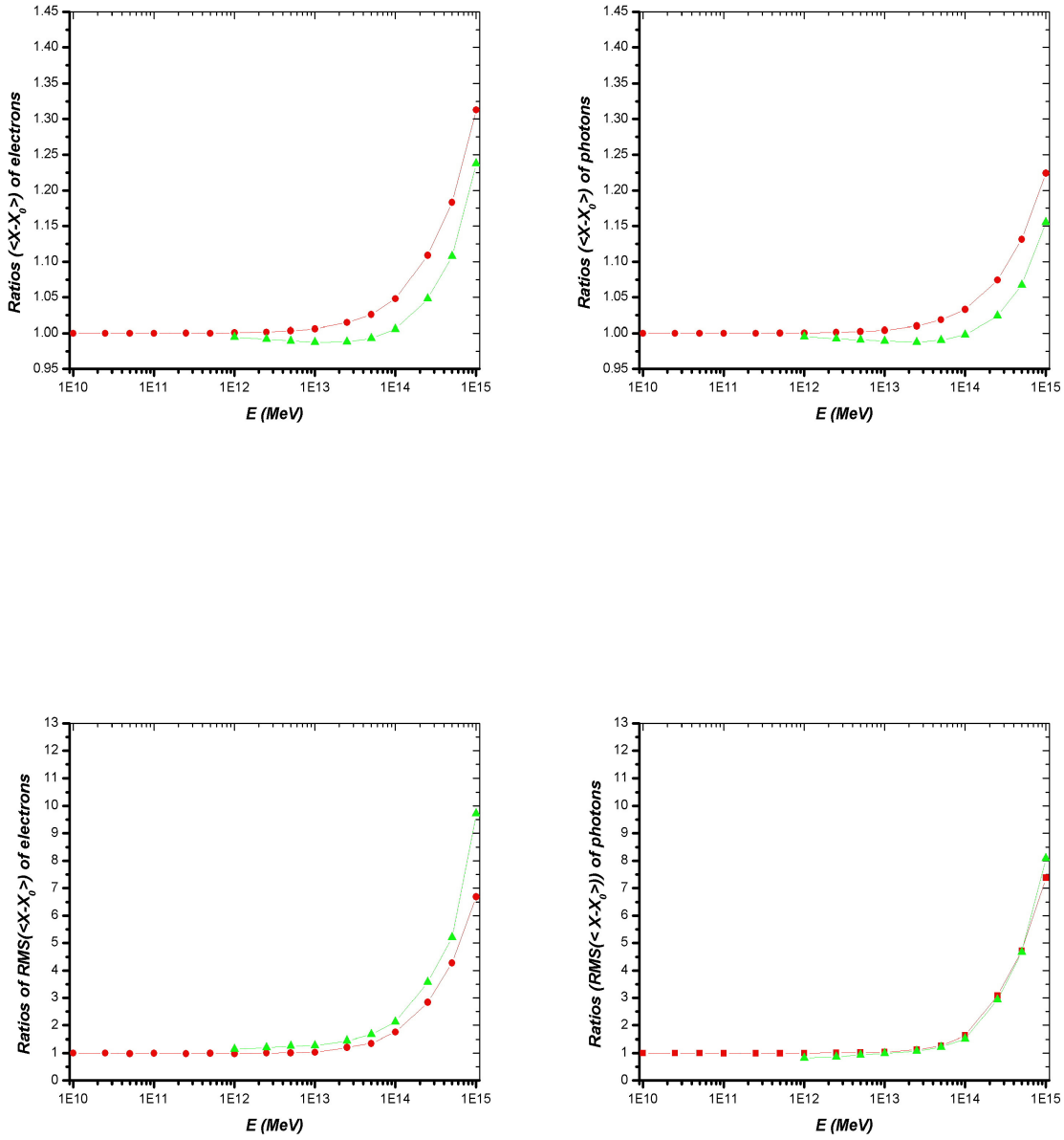

Figure 29b: Distributions of the ratios (green) between the LPM suppressed and LPM unsuppressed values of the mean (upper panels) and rms (lower panels) of $<X–X_0>$ for electrons (left panels) and photons (right panels). The red curves treat LPM suppression globally but ignore its effect on fractional energy sharing.

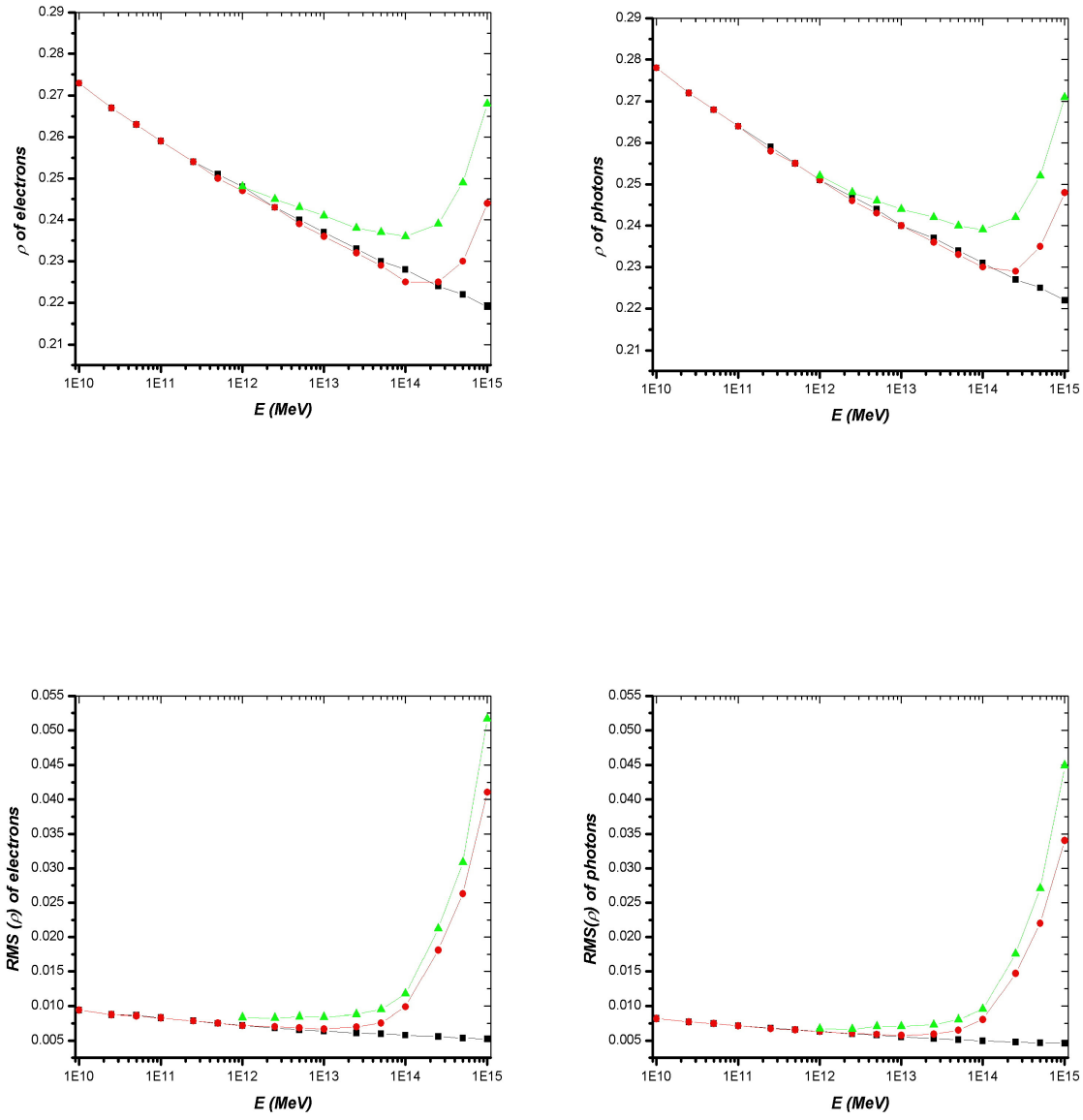

Figure 30a: Distributions of the mean values (upper panels) and rms values (lower panels) of ρ with LPM suppression (green) compared with no LPM suppression (black) for electrons (left panels) and for photons (right panels). The red curves treat LPM suppression globally but ignore its effect on fractional energy sharing.

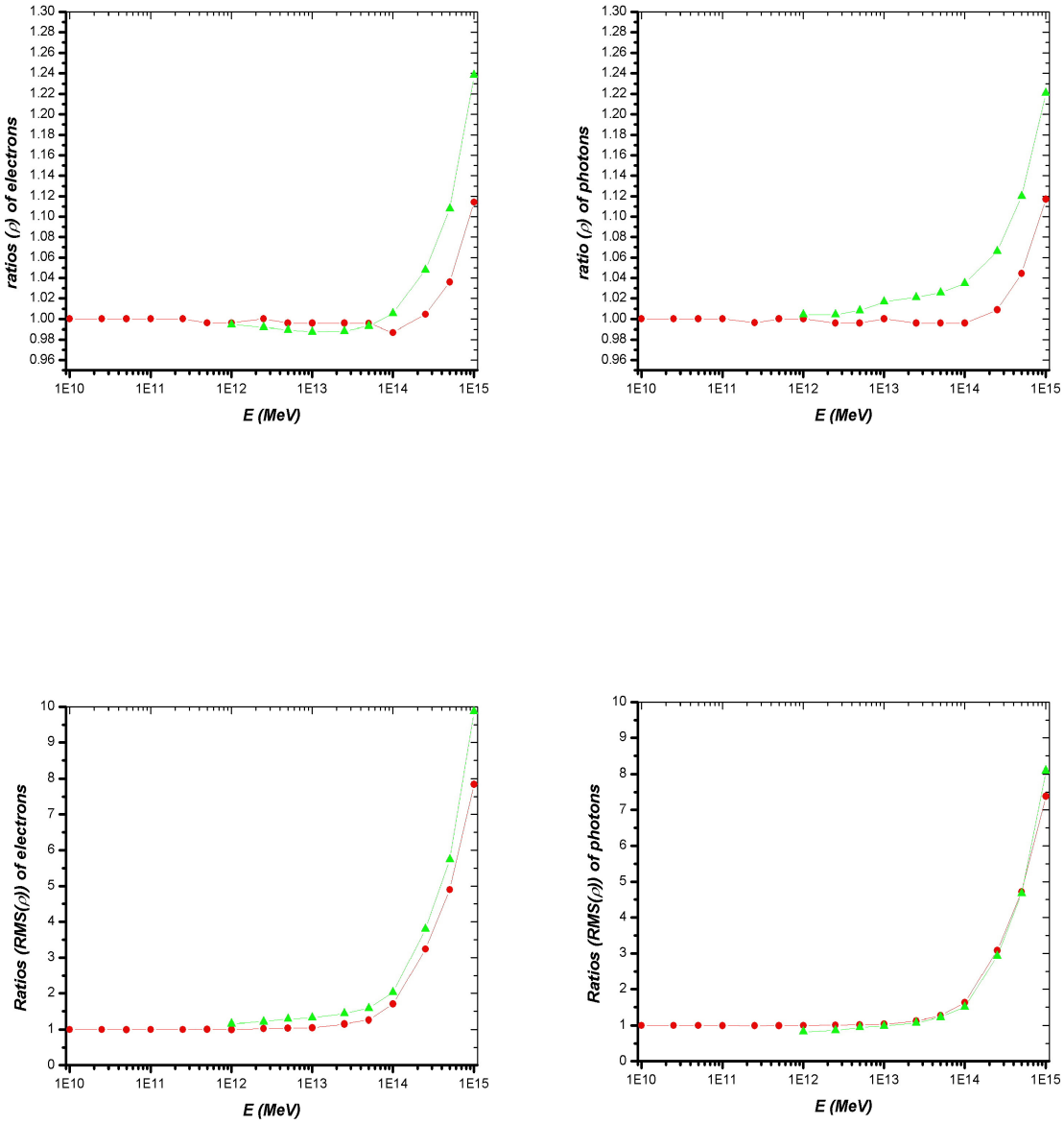

Figure 30b: Distributions of the ratios (green) between the LPM suppressed and LPM unsuppressed values of the mean (upper panels) and rms (lower panels) of ρ for electrons (left panels) and for photons (right panels). The red curves treat LPM suppression globally but ignore its effect on fractional energy sharing.

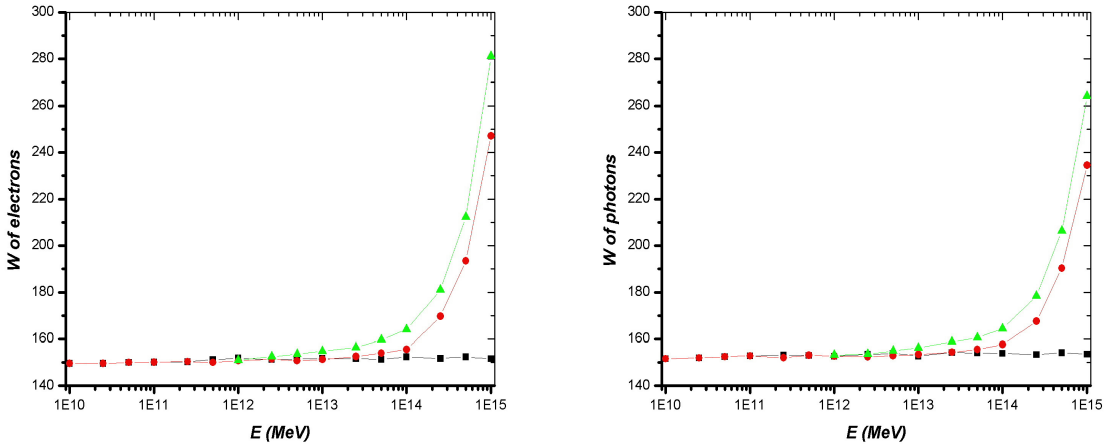

Figure 31a: Distributions of the values of $w = \langle\rho\rangle^2\langle\{\langle X\rangle - X_0\}\rangle$ with LPM suppression (green) compared with no LPM suppression (black) for electrons (left panels) and for photons (right panels). The red curves treat LPM suppression globally but ignore its effect on fractional energy sharing.

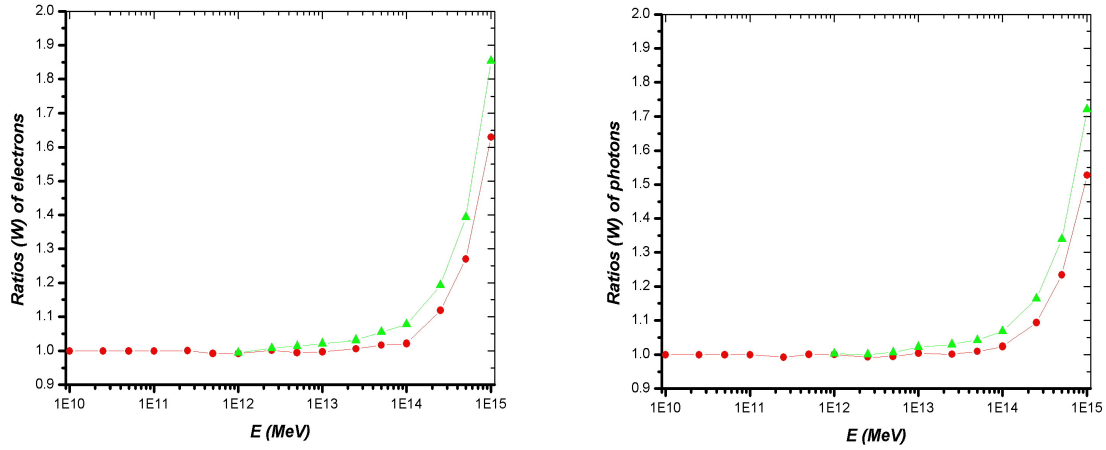

Figure 31b: Distributions of the ratios (green) between the LPM suppressed and LPM unsuppressed values of $w = \langle\rho\rangle^2\langle\{\langle X\rangle - X_0\}\rangle$ for electrons (left panels) and for photons (right panels). The red curves treat LPM suppression globally but ignore its effect on fractional energy sharing.

Energy sharing

The results obtained in the preceding section took into account the increase of the effective radiation length induced by LPM suppression (Figure 28) but ignored those of the different energy sharing between the electron and bremsstrahled photon or between the electron and positron of a converted photon (Figure 25). We now include the effect of the latter taking again $6.6En10^{-9}$ as a reference energy when comparing with the lead data of Figure 25. The results are shown in green in Figures 29 to 31. In the energy range considered here, LPM suppression is dominated by its effect on bremsstrahlung, that on pair creation is still small. Essentially, what happens is that the bremsstrahled photon takes away, on average, a larger fraction of the incident electron energy. As a photon shower does not start before 9/7 of a radiation length on average, LPM suppression will result in an increase of $<<X>-X_0>$.

It must be noted that the accuracy achieved in these calculations in at the percent level. In particular, the small decrease of the ratio (LPM suppressed to no LPM) of $<X-X_0>$ below unity seen in Figure 29b between 10^{13} and 10^{14} MeV is not significant. Another comment concerns the total thickness of the available atmosphere which has been assumed to be infinite in the present calculation. However, in practice, the atmosphere is limited to some 29 radiation lengths. Here, in particular in the case of LPM suppression, we deal with showers which extend well beyond this limit and which would be truncated in real life and end their development inside ground. As this effect is trivial and depends on the altitude of ground, we did not include it.

6. Summary and conclusion

Acknowledgements

References

1 K. Greisen, Phys. Rev. Lett. 16 (1966) 748,
Z.T. Zatsepin and V.A. Kuzmin, Zh. Eksp. Teor. Fiz. Pis'ma Red. 4 (1966) 144.

2 Abraham et al. (Auger Collaboration)rJ, Properties and performance of the prototype instrument of the Pierre Auger Observatory, Nuclear Instruments and Methods, A523 (2004) 50, and references therein.

J. Abraham et al. (Auger Collaboration), Upper limit on the cosmic ray photon flux above 1019eV using the surface detector of the Pierre Auger Observatory, Astroparticle Physics 29 (2008) 243.

3 Landau, L.D and Pomeranchuk, I.J., Dokl. Akad. Nauk. SSSR 92 535 (1953); Dokl. Akad. Nauk. SSSR 92, 735. These papers are available in English in The Collected Papers of L. D. Landau, Pergamon Press, 1965.

Migdal, A. B., Phys. Rev. 103, 1811 (1956).

4 P. N. Diep, Shower development: electrons and photons, longitudinal profile, VATLY Internal note 21, December 2008 and references therein.
5 Much of the material in this section is borrowed from P. Darriulat, 2008 Katmandou lectures on cosmic rays.
6 J. Abraham et al. (Auger Collaboration), Correlation of the highest energy cosmic rays with nearby extra-galactic objects, Science 318 (2007) 938.
7 K. Greisen, Proc. 9th Int. Cosmic Ray Conf. (1965) Inst. Phys. London, vol.2, p. 609.
A.M. Hillas, Ann. Rev. Astron. Astrophys., 22 (1984), 425.
8 Le Thi Huong , Galaxy collisions as possible sources of ultrahigh energy cosmics rays, Dissertation at the Hanoi University of Education, 2008
9 S. R. Klein, LBNL 41167, December 1997, arXiv:astro-ph/9712198v3 11 Dec 2000 and references therein. Much of the material in this section is borrowed from this paper.
10 P. L. Anthony et al., Phys. Rev. Lett. 75 (1995) 1949.
11. Particle Data Group, S. Eidelman, et al., Physics Letters B592 (2004) 1